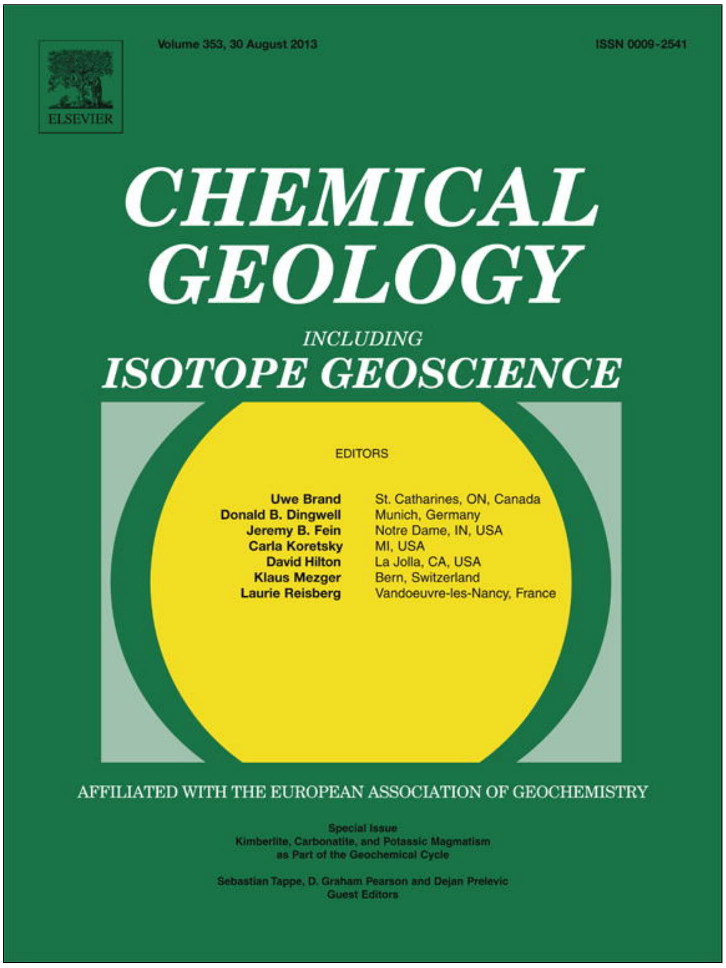
Volume 353, 30 August 2013
ISSN 0009-2541
ELSEVIER
CHEMICAL GEOLOGY
INCLUDING
ISOTOPE GEOSCIENCE
EDITORS
Uwe Brand St. Catharines, ON, Canada
Donald B. Dingwell Munich, Germany
Jeremy B. Fein Notre Dame, IN, USA
Carla Koretsky MI, USA
David Hilton La Jolla, CA, USA
Klaus Mezger Bern, Switzerland
Laurie Reisberg Vandoeuvre-les-Nancy, France
AFFILIATED WITH THE EUROPEAN ASSOCIATION OF GEOCHEMISTRY
Special Issue
Kimberlite, Carbonatite, and Potassic Magmatism
as Part of the Geochemical Cycle
Sebastian Tappe, D. Graham Pearson and Dejan Prelevic
Guest Editors

Chemical Geology 353 (2013) 112–131

Contents lists available at ScienceDirect

Chemical Geology

journal homepage: www.elsevier.com/locate/chemgeo

Trace-element partitioning in perovskite: Implications for the geochemistry of kimberlites and other mantle-derived undersaturated rocks☆

Anton R. Chakhmouradian [a],*, Ekaterina P. Reguir [a], Vadim S. Kamenetsky [b],
Victor V. Sharygin [c], Alexander V. Golovin [c]

[a] Department of Geological Sciences, University of Manitoba, 125 Dysart Road, Winnipeg, Manitoba, Canada, R3T 2N2
[b] School of Earth Sciences and Centre for Ore Deposit Research, University of Tasmania, Hobart, Australia, 7001
[c] Sobolev Institute of Geology and Mineralogy, Siberian Branch of the Russian Academy of Sciences, Prospect Ak. Koptyuga 3, Novosibirsk, Russia, 630090

ARTICLE INFO

Article history:
Accepted 4 January 2013
Available online 23 January 2013

Keywords:
Perovskite
Kimberlite
Katungite
Element partitioning
Crystal fractionation
Magma evolution

ABSTRACT

Perovskite is a common groundmass phase in many mantle-derived undersaturated rocks (e.g., kimberlites), serving as an important repository for rare-earth elements (REE), high-field-strength elements (especially, Ti, Nb and Ta), Th and U. Perovskite-groundmass partition coefficients, calculated for samples of hypabyssal kimberlite from the Chicken Park (Colorado), Iron Mountain (Wyoming) and Udachnaya East (Russia) are largely consistent with those calculated for perovskite from katungite (potassic olivine melilitite) lava from Bunyaruguru, Uganda. The major and trace elements, analyzed by electron-microprobe and laser-probe techniques, can be grouped into strongly incompatible ($D_X \ll 0.1$: K, Rb, Zn, Ba, Al), moderately incompatible ($D_X = 0.1$–0.5: Mn, Ga, Sc, V, Fe), compatible ($D_X = 1.0$–5.0: Ca, Sr, Hf, heavy REE), and strongly compatible ($D_X > 5.0$: Y, light- to mid-range REE, Th, U, Ti, Nb, Ta). Sodium gives a wide range of partitioning values in the kimberlitic perovskite, all of which are higher than the Na value for the katungite ($D_{Na} = 0.19$). This discrepancy is interpreted to indicate loss of Na from the kimberlitic magma during its emplacement, resulting in low Na levels in the groundmass and overestimated partition coefficients. The calculated Pb values corrected for U–Th decay are also many times higher in the kimberlitic perovskite relative to the katungite ($D_{Pb} = 0.3$); the latter value is considered a better estimate because it was not affected by U–Th decay and is in better accord with the partitioning data for other divalent cations. Notably, perovskite has a higher affinity for light REE (LREE), Ho, Ta, Hf and Th relative to heavy REE (HREE), Y, Nb, Zr and U, respectively. Decoupling is particularly strong in the LREE-HREE, Th-U and Nb-Ta pairs, and will produce a noticeable effect on the composition of magma precipitating perovskite even at small degrees of fractionation. Such effects are not observed in kimberlites, even though fractionation of other minerals (notably, olivine) probably does play an important role in the evolution of kimberlites, as demonstrated in the present work on the basis of published data. Perovskite in kimberlites commonly develops a zoning pattern involving a rim-ward decrease in Th/U ratio, Na, REE, Th and Ta contents, and an increase in Nb/Ta value, which can be explained by gradual depletion of the host magma in these elements due to their early sequestration in the core of perovskite crystals and, possibly, Na loss (see above). There are also cases (e.g., Lac de Gras kimberlites) where perovskite develops a discontinuous Nb–Fe–Zr-rich rim. These evolved compositions plot away from the normal zoning trend described above owing to their low Na content for the given level of REE enrichment, indicating that a significant proportion of the latter elements is incorporated in this perovskite as REE(Fe,Al)O_3. Petrographic observations, combined with the published data and lack of any spectroscopic evidence for the presence of water in this perovskite, indicate that this type of zoning formed due to the loss of a volatile phase from the kimberlitic magma, accompanied by perovskite fragmentation and followed by reaction of perovskite fragments with an evolved trace-element-rich melt.

1. Introduction

The origin and evolution of kimberlites is a contentious area of igneous petrology, not to the least because the composition of their parental magmas remains poorly understood. In the past decade, a number of studies have been undertaken to estimate the composition and fluid regime of kimberlitic magmas using whole-rock geochemical

---

☆ This work is dedicated to Roger H. Mitchell in recognition of his career-long contribution to the petrology of kimberlites and structural study of perovskites.

* Corresponding author.
E-mail address: chakhmou@cc.umanitoba.ca (A.R. Chakhmouradian).

0009-2541/$ – see front matter © 2013 Elsevier B.V. All rights reserved.
http://dx.doi.org/10.1016/j.chemgeo.2013.01.007

data and experimental constraints (Price et al., 2000; le Roex et al., 2003; Keshav et al., 2005; Kjarsgaard et al., 2009; Patterson et al., 2009). The published estimates differ by a factor of two for such key components as CaO, MgO and FeO_{total}, and significantly for most elements present at the level of $n \times 10^3$–10^4 ppm (e.g., K, Al and Ti). This work has been challenged recently as not giving adequate consideration to the effects of subsolidus processes (Sparks et al., 2009; Brooker et al., 2011), or the abundance of alkali- and Cl-rich phases in some kimberlites (Kamenetsky et al., 2004). Several recent studies have also discussed the trace-element budget of primordial melts, either from the standpoint of peridotite-melt element partitioning (Brey et al., 2008), or based on the consistency of certain element ratios in kimberlites worldwide (le Roex et al., 2003; Paton et al., 2009).

One promising, although essentially unexplored, approach to addressing some of the outstanding problems of kimberlite petrogenesis is to examine the character of trace-element partitioning in minerals

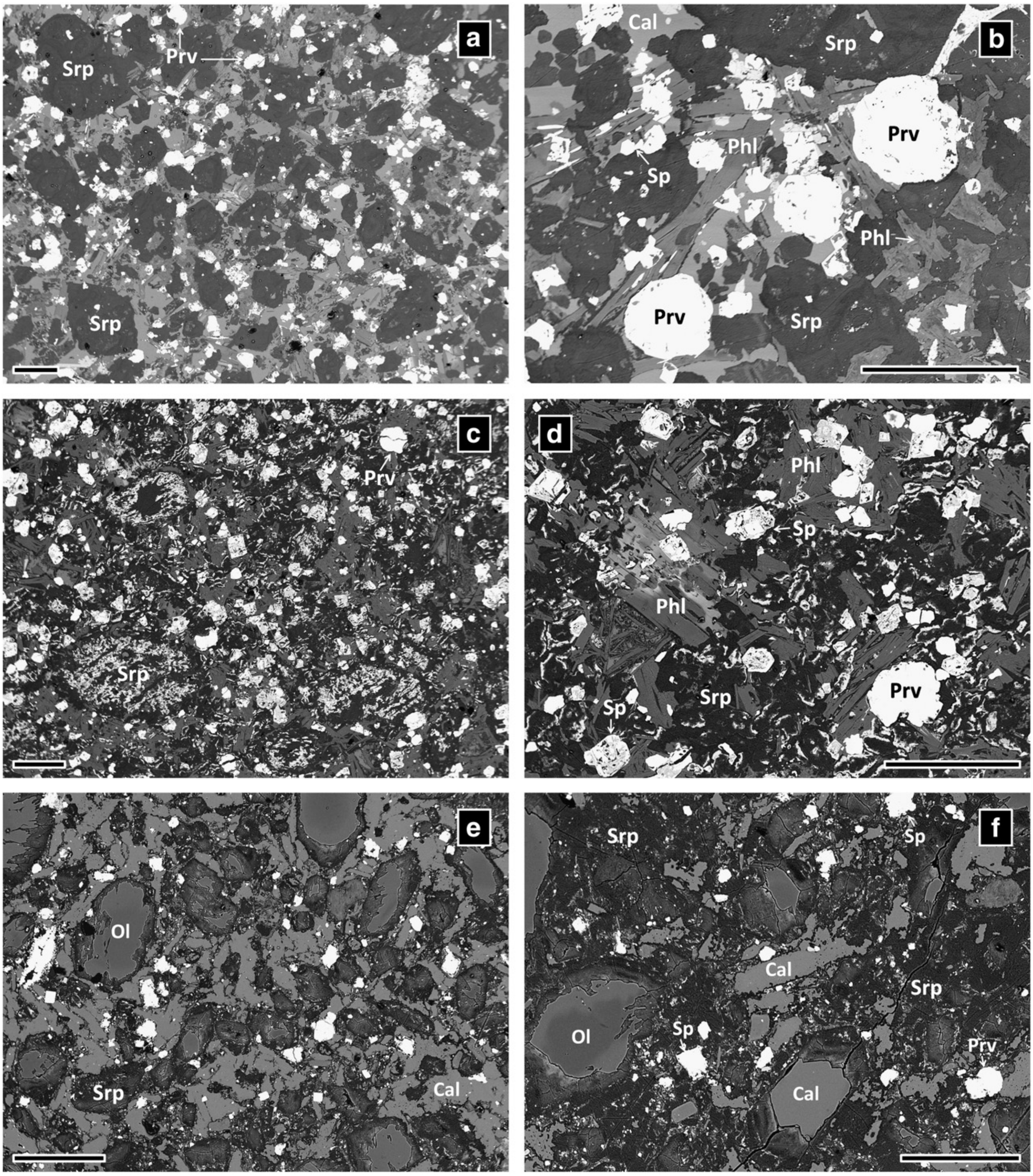

Fig. 1. Textural characteristics of kimberlites examined in the present work (BSE images) and typical paragenetic relations between perovskite (Prv) and other groundmass minerals (Srp = serpentine, Sp = spinel-group minerals, Phl = phlogopite, Cal = calcite, Ol = olivine): (a and b) Chicken Park; (c and d) Iron Mountain; (e and f) Udachnaya East. Scale bar is 200 μm for all images.

that: (a) are reasonably common in kimberlites; (2) can accommodate a broad range of elements in their crystal structure; (c) are amenable to *in situ* trace-element analysis (i.e., larger than ~50 μm); (d) have been well-characterized paragenetically and structurally to permit treatment of the observed compositional variations in a petrogenetic context. One mineral that meets all of the above criteria is perovskite (ideally $CaTiO_3$), occurring as a widespread and in some cases, volumetrically significant groundmass phase in kimberlites (Chakhmouradian and Mitchell, 2000). Uranium – Th – Pb geochronology of this mineral using a variety of mass-spectrometric techniques has become an essential aspect of kimberlite research (Heaman and Kjarsgaard, 2000; Batumike et al., 2008; Li et al., 2010; Donatti-Filho et al., 2013–this volume; Tappe et al., 2012; Wu et al., 2013–this issue). In addition, the importance of perovskite as a source of isotopic (Sr, Nd and Pb) evidence for unraveling the mantle sources of kimberlites has been increasingly recognized in recent years (Paton et al., 2007; Woodhead et al., 2009; Yang et al., 2009; Wu et al., 2010, 2013–this issue; Tappe et al., 2012).

To our knowledge, the only experimental attempt to evaluate the partitioning behavior of perovskite in kimberlitic magma was made by Beyer et al. (2013–this volume). Melluso et al. (2008) calculated perovskite-groundmass partition coefficients for a number of kimberlite and kamafugite occurrences in Brazil; however, their estimates are based on a very limited set of analytical data, associated with large errors, and report unrealistically high partition coefficients for some of the elements (e.g., ~1.0 for Rb vs. 1.9 for Sr). Using the lattice-strain equation of Blundy and Wood (1994), which relates the radii of substituting cations to their partition coefficients, it is easy to see that Rb^{+}, which is ~30% larger than Sr^{2+} in an eight-fold coordination (Shannon, 1976), should have a partition coefficient in perovskite about three orders of magnitude (!) smaller than the Sr value. To our knowledge, the only other partitioning study of relevance to mantle-derived primitive magmas is that by Onuma et al. (1981), which unfortunately lacks data for such key elements as Rb, Sr, Ba, Pb, Y, Zr, Nb and Ta. Clearly, a better knowledge of the trace-element composition of groundmass perovskite is required to model the effects of its crystallization on magma evolution.

The primary objectives of the present work were to improve the current understanding of element partitioning in perovskite using a representative set of analytical data and to evaluate the effects of perovskite fractionation in undersaturated mantle-derived melts. For this purpose, we used a carefully selected set of kimberlite samples, and one sample of fresh katungite lava from Uganda in the East African Rift. Katungites are (ultra)potassic (atomic K/Na = 1.0–8.5; $K_2O/Na_2O = 0.9–7.6$) ultramafic members of the kamafugite clan (Foley et al., 1987) showing distinct trace-element similarities to archetypal or Group 1 kimberlites (Mitchell and Bell, 1976; see also Section 4.2), but restricted in occurrence to rift settings (Holmes, 1950; Tappe et al., 2003). Other reasons why the Ugandan katungite was chosen was its young age (<50 Ka: Boven et al., 1998) and petrographic characteristics (see below),

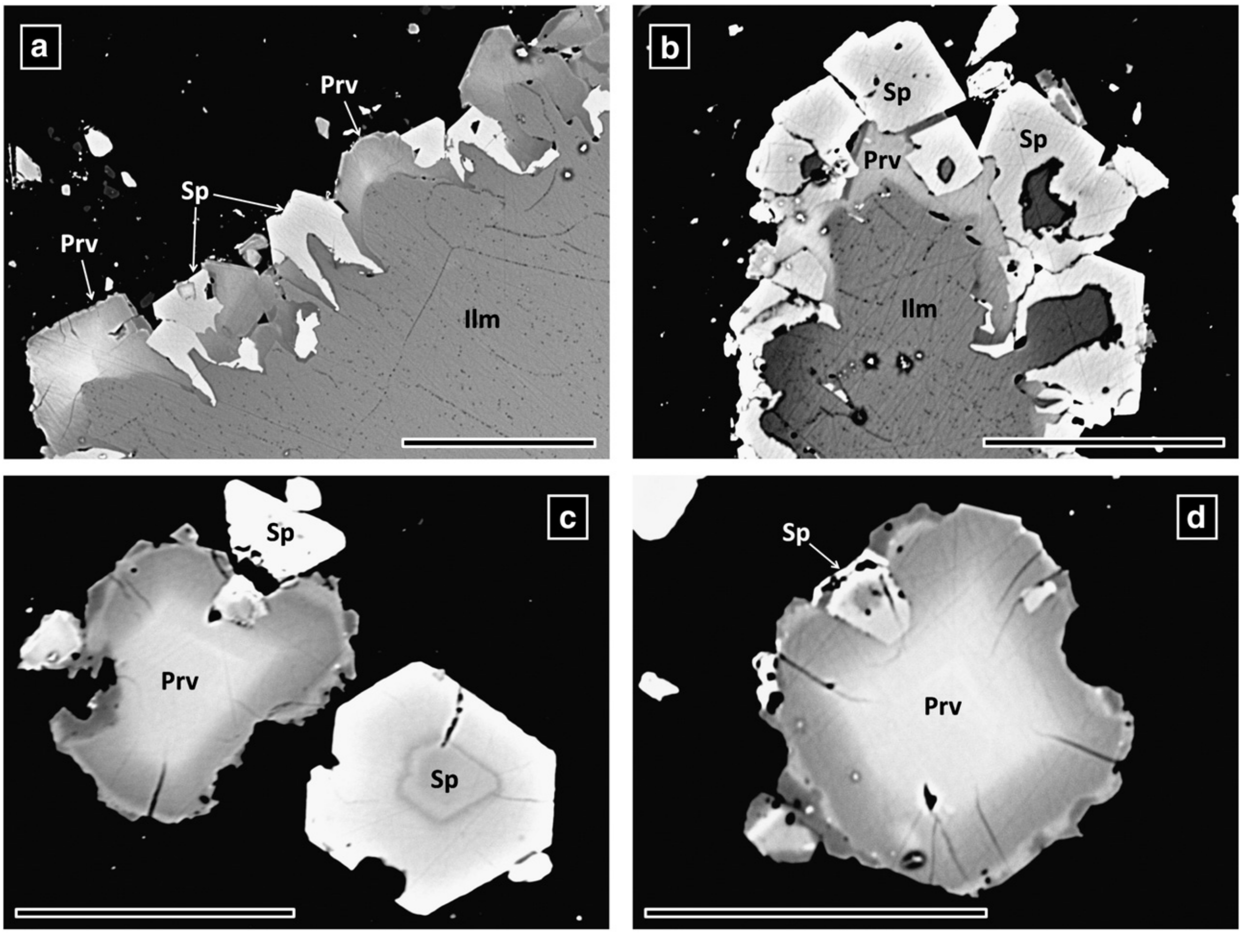

Fig. 2. Paragenesis, morphology and zoning of groundmass perovskite (Prv) in kimberlites and katungite (BSE images); scale bar is 50 μm for all images. (a and b) reaction-induced rims around ilmenite macrocrysts (Ilm) composed of semi-euhedral perovskite and spinels in the Udachnaya East kimberlites; (c and d) normally zoned perovskite in the Udachnaya East kimberlites, note close paragenetic association of perovskite with spinels; (e) normally zoned perovskite in the Chicken Park kimberlite; (f) early perovskite (grey) fragmented, resorbed and partially mantled by Nb – Fe-rich perovskite (white), Grizzly; (g) euhedral crystals of perovskite embedded in a glassy matrix and melilite microphenocrysts (Mel) in the Bunyaruguru katungite; (h) oscillatory zoning in the Bunyaruguru perovskite.

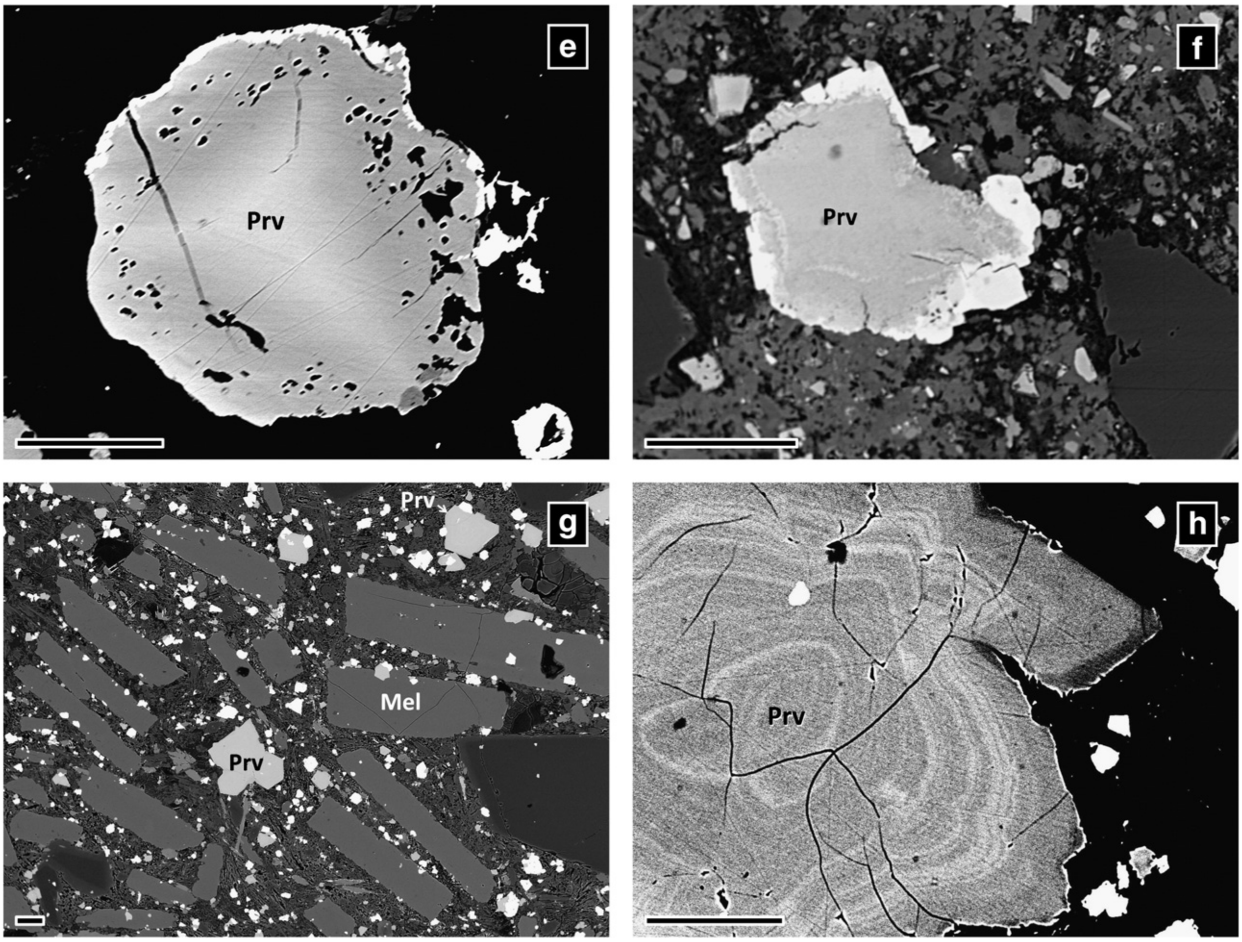

Fig. 2 (*continued*).

indicating that the trace-element budget of this rock and its constituent minerals has not been significantly modified by devolatilization, wall-rock metasomatism, or U–Th decay, which has important implications for the assessment of element partitioning in perovskite (see Section 5.2).

2. Material and methods

Ten samples of hypabyssal kimberlite from Chicken Park (Colorado), Iron Mountain (Wyoming), Udachnaya East (Daldyn-Alakit field, Siberia) and the Grizzly pipe (Lac de Gras field, Northwest Territories, Canada), and one sample of katungite (potassic olivine melilitite) from the Bunyaruguru volcanic field in the Toro Ankole igneous province (south-western Uganda) were selected for a detailed study. The samples were characterized by polarized light microscopy and back-scattered-electron (BSE) imaging to select areas for further analysis, assess the morphological variability of perovskite, and estimate its modal abundance.

The major-element composition of perovskite was determined by wavelength-dispersive X-ray spectrometry (WDS) using a CAMECA SX-100 electron-microprobe (University of Manitoba, Canada) operated at 15 kV and 20 nA with a beam size of 1 μm. The following natural and synthetic standards were employed for calibration: albite (Na); diopside (Si, Ca); orthoclase (K); titanite (Ti); andalusite (Al); $NaBa_2Nb_5O_{15}$ (Ba, Nb); fayalite (Fe); spessartine (Mn); $SrTiO_3$ (Sr); zircon (Zr); light-rare-earth orthophosphates (La, Ce, Pr, Nd and Sm); ThO_2 (Th); UO_2 (U); $MnNb_2Ta_2O_9$ (Ta). Silicon, K, Mn, Ba and U were sought, but found not to be present above their limit of detection by WDS (ca. 150, 200, 500, 2000 and 800 ppm, respectively) in any of the samples. Analytical lines and other WDS instrumental parameters are summarized in Appendix 1. In total, 227 WDS analyses were acquired.

The trace-element composition of perovskite was determined by laser-ablation inductively-coupled-plasma mass-spectrometry (LA-ICP-MS) using a New Wave UP-213 ablation system coupled with an Agilent 4500 quadrupole mass-spectrometer at the University of Tasmania, Australia. Matching reflected-light and BSE images of the perovskite grains previously analyzed by WDS were used to position accurately the laser beam and avoid inclusions, fractures and grain boundaries. The analyses were performed with a laser beam focused to a 25-μm spot at a pulse frequency of 5 Hz and energy density on the sample of 2.5 J/cm^2. Other relevant instrumental parameters are listed in Appendix 1. After taking into account potential spectral overlaps and molecular interferences, the following isotopes were chosen for analysis: ^{24}Mg, ^{27}Al, ^{39}K, ^{43}Ca, ^{45}Sc, ^{51}V, ^{55}Mn, ^{57}Fe, ^{66}Zn, ^{69}Ga, ^{88}Sr, ^{89}Y, ^{9}Zr, ^{93}Nb, ^{133}Cs, ^{137}Ba, ^{139}La, ^{140}Ce, ^{141}Pr, ^{146}Nd, ^{147}Sm, ^{153}Eu, ^{157}Gd, ^{159}Tb, ^{163}Dy, ^{165}Ho, ^{166}Er, ^{169}Tm, ^{172}Yb, ^{175}Lu, ^{178}Hf, ^{181}Ta, ^{208}Pb, ^{232}Th and ^{238}U. Synthetic glass standard NIST SRM 612 (Pearce et al., 1997) was employed for calibration, and natural reference material BCR-2 (Wilson, 1997) was measured as an unknown and monitored for data quality control. The measured concentrations do not deviate by more than 10% of the reference value for any of the elements, and for 60% of the elements, the magnitude of deviation is less than 6%. All signal processing and data reduction were carried out using an in-house software developed at the University of Tasmania. The Ca concentrations determined by

Table 1
Representative major-element compositions (WDS data) and formulae of perovskite from kimberlites (1–13) and katungite (14).

Wt.%	1	ESD	2	ESD	3	ESD	4	ESD	5	ESD	6	ESD	7	ESD	8	ESD	9	ESD	10	11	12	13	14	ESD
Na_2O	0.38	0.02	0.22	0.10	0.49	0.04	0.27	0.07	0.85	0.12	0.58	0.19	0.89	0.10	0.45	0.11	0.43	0.07	0.39	0.67	1.10	1.00	0.28	0.03
CaO	38.00	0.21	39.45	0.52	37.08	0.35	38.29	0.55	35.16	0.70	37.15	0.97	35.26	0.51	37.34	0.67	35.03	0.74	35.13	33.66	31.83	32.42	38.65	0.25
SrO	0.17	0.02	0.38	0.24	0.20	0.04	0.57	0.37	0.19	0.04	0.18	0.05	0.18	0.05	0.19	0.03	0.22	0.04	0.25	0.26	0.19	0.21	0.41	0.05
La_2O_3	0.53	0.06	0.25	0.15	0.85	0.09	0.68	0.09	1.08	0.12	0.87	0.23	1.13	0.14	0.96	0.14	1.58	0.12	1.78	1.45	2.03	1.46	0.65	0.05
Ce_2O_3	1.54	0.07	0.50	0.40	2.19	0.14	1.06	0.50	3.02	0.22	1.93	0.67	3.01	0.22	2.06	0.52	4.00	0.21	4.05	4.17	4.64	3.67	1.57	0.14
Pr_2O_3	0.19	0.04	0.06	0.06	0.18	0.06	0.13	0.12	0.24	0.10	0.12	0.11	0.24	0.08	0.11	0.11	0.37	0.07	0.29	0.35	0.40	0.31	0.32	0.10
Nd_2O_3	0.69	0.07	0.20	0.24	0.80	0.08	0.37	0.22	1.13	0.13	0.67	0.25	1.09	0.15	0.67	0.25	1.28	0.07	1.29	1.28	1.46	1.02	0.60	0.07
Sm_2O_3	0.09	0.04	0.07	0.05	0.12	0.05	0.06	0.04	0.17	0.08	0.14	0.08	0.12	0.05	0.09	0.09	0.07	0.04	0.03	0.15	0.17	0.06	0.09	0.07
ThO_2	0.29	0.04	0.04	0.06	0.54	0.07	0.04	0.08	1.05	0.66	0.05	0.06	1.07	0.29	0.02	0.04	0.97	0.87	0.23	1.61	0.85	1.18	0.15	0.05
Al_2O_3	0.34	0.03	0.31	0.03	0.28	0.01	0.34	0.04	0.33	0.07	0.23	0.13	0.31	0.03	0.42	0.04	0.54	0.04	0.57	0.52	0.49	0.40	0.18	0.02
Fe_2O_3	1.18	0.09	1.37	0.29	1.70	0.11	1.84	0.24	1.44	0.24	1.33	0.26	1.38	0.08	1.58	0.18	2.55	0.09	3.15	3.27	5.18	6.13	1.48	0.49
TiO_2	55.57	0.11	55.80	0.53	53.91	0.46	54.02	0.56	52.74	1.02	54.12	0.76	53.34	0.46	53.63	0.53	49.37	0.39	47.67	44.62	38.62	34.67	54.19	0.11
ZrO_2	n.d.	–	n.d.	–	n.d.	–	n.d.	–	0.17	0.11	0.19	0.09	0.12	0.04	0.23	0.08	0.17	0.06	0.37	0.60	0.96	1.03	n.d.	–
Nb_2O_5	0.43	0.04	0.62	0.21	0.87	0.11	1.12	0.34	1.57	0.49	1.57	0.46	1.47	0.24	1.51	0.21	3.12	0.50	4.49	6.92	12.69	16.58	0.42	0.03
Ta_2O_5	n.d.	–	n.d.	–	n.d.	–	n.d.	–	0.28	0.17	0.12	0.12	0.39	0.11	0.02	0.03	0.48	0.17	0.04	1.02	0.38	0.59	n.d.	–
Total	99.40		99.27		99.21		98.79		99.42		99.25		100.00		99.28		100.18		99.73	100.55	100.99	100.73	98.99	
Atoms per formula unit calculated to 3 atoms of oxygen																								
Na	0.017		0.010		0.022		0.012		0.039		0.026		0.041		0.020		0.020		0.018	0.032	0.053	0.049	0.013	
Ca	0.947		0.975		0.936		0.961		0.898		0.934		0.895		0.939		0.904		0.910	0.884	0.847	0.869	0.973	
Sr	0.002		0.005		0.003		0.008		0.003		0.002		0.002		0.003		0.003		0.004	0.004	0.003	0.003	0.006	
La	0.005		0.002		0.007		0.006		0.009		0.008		0.010		0.008		0.014		0.016	0.013	0.019	0.013	0.006	
Ce	0.013		0.004		0.019		0.009		0.026		0.017		0.026		0.018		0.035		0.036	0.037	0.042	0.034	0.013	
Pr	0.002		–		0.002		0.001		0.002		0.001		0.002		0.001		0.003		0.003	0.003	0.004	0.003	0.003	
Nd	0.006		0.002		0.007		0.003		0.010		0.006		0.009		0.006		0.011		0.011	0.011	0.013	0.009	0.005	
Sm	0.001		0.001		0.001		0.001		0.001		0.001		0.001		0.001		0.001		–	0.001	0.001	0.001	0.001	
Th	0.002		–		0.003		–		0.006		–		0.006		–		0.005		0.001	0.009	0.005	0.007	0.001	
ΣA cations	0.995		0.999		1.000		1.001		0.994		0.995		0.992		0.996		0.996		0.999	0.994	0.987	0.988	1.021	
Al	0.009		0.008		0.008		0.009		0.009		0.006		0.009		0.012		0.015		0.016	0.015	0.014	0.012	0.005	
Fe^{3+}	0.021		0.024		0.030		0.033		0.026		0.023		0.025		0.028		0.046		0.057	0.060	0.097	0.115	0.026	
Ti	0.972		0.968		0.955		0.951		0.946		0.955		0.950		0.947		0.894		0.867	0.822	0.721	0.653	0.957	
Zr	–		–		–		–		0.002		0.002		0.001		0.003		0.002		0.004	0.007	0.012	0.013	–	
Nb	0.005		0.006		0.009		0.012		0.017		0.017		0.016		0.016		0.034		0.049	0.077	0.143	0.188	0.004	
Ta	–		–		–		–		0.002		0.001		0.003		–		0.003		–	0.007	0.003	0.004	–	
ΣB cations	1.007		1.006		1.002		1.005		1.002		1.004		1.004		1.006		0.994		0.993	0.988	0.990	0.985	0.992	

n.d. = not detected. Data: (1) average core ($n=7$) and (2) rim ($n=8$), Chicken Park (outcrop); (3) average core ($n=12$) and (4) rim ($n=8$), Iron Mountain (outcrop); (5) average core ($n=19$) and (6) rim ($n=12$), Udachnaya East (depth 128 m); (7) average core ($n=9$) and (8) rim ($n=7$), Udachnaya East (depth 420 m); (9) average core ($n=4$) and (10–13) individual spot analyses of the rim, Grizzly; (14) average bulk grain ($n=11$), Bunyaruguru (outcrop).

WDS were used as an internal standard for all analyses. Out of the 110 trace-element analyses acquired, 22 showed evidence of “signal contamination” due to the presence of inclusions in the ablated area and were discarded.

Raman spectra were recorded using an automated LabRAM ARAMIS instrument (HORIBA Jobin-Yvon) at the University of Manitoba equipped with a multichannel electronically cooled charge-coupled device detector, motorized x–y–z stage and low-noise mpc6000 laser emitting at 532 nm (Laser Quantum) with a nominal power output of 50 mW. The instrument was operated in confocal mode; an Olympus microscope coupled to the spectrometer was used to focus the laser beam on the sample surface and collect the resultant Raman signal. The spectra were collected with a diffraction grating of 1800 grooves/mm; other instrumental parameters (data collection times, slit width, etc.) were optimized by performing multiple measurements on the same sample. The spectrometer was calibrated prior to each series of measurements using the 520.7 cm^{-1} signal from a synthetic Si standard.

Selected whole-rock samples were analyzed for their major- and trace-element composition at Activation Laboratories Ltd. (Ancaster, Ontario). The samples were pulverized, fused with Li meta- and tetraborate fluxes and analyzed by inductively-coupled-plasma mass-spectrometry (ICP-MS) for major- and trace elements using a PerkinElmer SCIEX ELAN instrument.

3. Compositional variation of perovskite

3.1. Petrography

All kimberlite samples examined in the present work contain relatively large (typically, 30–100 μm) sub- to euhedral perovskite crystals enclosed in a fine-grained calcite-spinel-serpentine (± olivine ± phlogopite ± apatite ± monticellite) groundmass (Fig. 1) and lacking any evidence of subsolidus alteration (cf. Chakhmouradian and Mitchell, 2000; Yang et al., 2009). Some of the samples from Udachnaya East also contain intricate intergrowths of euhedral perovskite and Fe – Ti-rich spinel mantling Mg – Cr-rich macrocrystic ilmenite (Fig. 2a and b). With the exception of the Grizzly sample, the groundmass population in all examined kimberlites is dominated by crystals showing a simple zoning pattern consisting of a high-AZ (AZ = average atomic number) core grading into a low-AZ rim (Fig. 2c–e). Some perovskite crystals from the Udachnaya East kimberlites show a very narrow (<5 μm) discontinuous overgrowth of very low-AZ material (Fig. 2d). Crystals from the Grizzly kimberlite differ from the rest of the samples in comprising a large resorbed and fragmented low-AZ core encrusted with coalescing minute (5–15 μm across) cubes of high-AZ perovskite; the rim is discontinuous and core-rim boundary is sharp (Fig. 2f).

The katungite sample (Bunyaruguru) is fine-grained, non-vesicular and free of xenocrysts. It contains numerous euhedral and twinned crystals of perovskite up to 300 μm across set in a fresh glassy groundmass or included in flow-aligned melilite microphenocrysts (Fig. 2g). In BSE images, the crystals exhibit subtle oscillatory zoning (Fig. 2h). Associated groundmass phases include apatite and groundmass spinels ranging from early Mg – Al-rich chromite to Fe – Ti-rich compositions.

3.2. Major- and trace-element composition of perovskite

The complete set of WDS and LA-ICP-MS data is presented in Appendix 2; representative major- and trace-element compositions are given in Tables 1 and 2, respectively. The Chicken Park, Iron Mountain and Udachnaya East samples contain relatively minor levels of substituent elements (i.e. ≥85 mol% $CaTiO_3$, Prv). The most

Table 2
Trace-element compositional variation of perovskite from kimberlites and katungite.

ppm	Chicken Park		Iron Mountain		Ud. East-128		Ud. East-420		Grizzly (core)		Bunyaruguru	
	Min	Max	Min	Max	Min	Max	Min	Max	Min	Max	Min	Max
K	120	178	111	225	12	285	151	232	209	429	203	330
Rb	b.d.	0.14	b.d.	0.30	b.d.	0.35	b.d.	1.25	b.d.	0.34	b.d.	0.38
Mn	240	282	169	239	209	280	234	295	110	152	124	133
Zn	b.d.	3.1	b.d.	7.1	b.d.	6.8	b.d.	10.0	2.3	2.8	0.52	4.0
Sr	1152	1518	1724	1879	1298	1644	1342	1560	1666	2024	3339	3575
Ba	3.6	15.6	13	80	3.3	13	7.7	21	12	33	18	22
Pb	47.6	200	92	188	53	361	108	384	19	118	2.7	3.6
Y	181	233	170	214	170	258	207	256	81	94	86	95
La	2978	4521	6162	7357	6102	9817	6912	9493	12583	15062	5113	5492
Ce	8162	12222	13276	17424	13955	25267	16796	25234	29119	35688	12354	13588
Pr	1000	1442	1390	1865	1498	2850	1837	2801	2966	3616	1329	1462
Nd	3909	5566	4897	6637	5081	10194	6473	9977	9444	11413	4722	5187
Sm	511	712	567	729	585	1152	725	1107	752	860	478	517
Eu	115	154	126	161	123	225	147	221	134	140	99	108
Gd	256	338	274	327	263	515	340	464	255	266	182	193
Tb	22	30	23	29	22	41	27	39	16	19	13	15
Dy	90	117	81	109	87	155	107	141	53	65	46	51
Ho	11	14	11	13	9.4	17	11	16	5.4	6.2	5.0	5.5
Er	18	23	15	22	14	25	20	25	7.9	9.8	7.6	9.2
Tm	1.62	2.21	0.93	1.81	1.32	3.37	1.36	1.84	0.37	0.77	0.67	0.80
Yb	5.6	8.4	3.9	7.0	3.8	11	4.6	8.0	2.5	3.8	2.8	3.3
Lu	0.46	0.66	0.40	1.01	0.34	0.79	0.37	0.67	0.15	0.23	0.26	0.37
Th	708	2780	2149	4376	1238	10731	2416	9464	1478	17241	1065	1249
U	66	86	72	114	132	211	161	263	81	95	42	47
Mg	352	715	370	803	415	1828	428	677	1051	1172	226	359
Al	1360	1651	1254	1455	825	1874	685	1704	2844	3262	929	1105
Sc	4.3	6.7	2.1	6.2	2.0	15	b.d.	9.3	20	45	3.0	3.6
Fe	8305	9607	11395	15003	7415	12248	8167	10873	21220	26342	11629	12927
Ga	0.61	2.57	0.80	2.63	0.25	3.70	0.83	2.42	1.49	1.82	0.61	1.19
V	104	116	99	114	79	131	92	157	84	111	111	121
Zr	189	372	204	307	240	983	438	1008	881	2454	149	171
Hf	8.7	18	10	16	9.3	61	25	57	58	119	7.6	8.5
Nb	2585	3154	3957	6195	5353	9897	7340	11555	15599	29410	2826	3014
Ta	498	715	720	1126	841	2832	1213	2996	2284	5899	362	396

b.d. = below detection.

significant substituents in the Ca site are rare-earth elements (REE) and Na, amounting to ~10 mol% $Na_{0.5}REE_{0.5}TiO_3$ (loparite component, Lop) in the Udachnaya East perovskite. Near-stoichiometric cation totals in the Ca site and a good negative correlation between the Ca and 3Na + Th + REE values (Fig. 3a) indicate that the proportion of vacancies and hence, the relative contribution of such hypothetical end-member components as $REE_{0.67}TiO_3$ and $Th_{0.5}TiO_3$ is negligible. A coupled substitution of Ti by Nb + Fe^{3+} accounts for up to 7 mol% $CaNb_{0.5}Fe_{0.5}O_3$ (latrappite, Ltr) in some of the kimberlite varieties from Udachnaya East. The Grizzly perovskite contains much higher levels of substituent elements in the Ti site (54–86 mol% Prv; up to 25 mol% Ltr and 10 mol% Lop). None of the other end-member components (in particular, $NaNbO_3$, $SrTiO_3$, $CaZrO_3$, $REEFeO_3$ and $REEAlO_3$) exceed 3 mol% in any of the samples. The Bunyaruguru perovskite is compositionally similar to the most Na–REE–Th–Fe–Nb-poor samples from the kimberlites (≥93 mol% Prv at ≤3 mol%

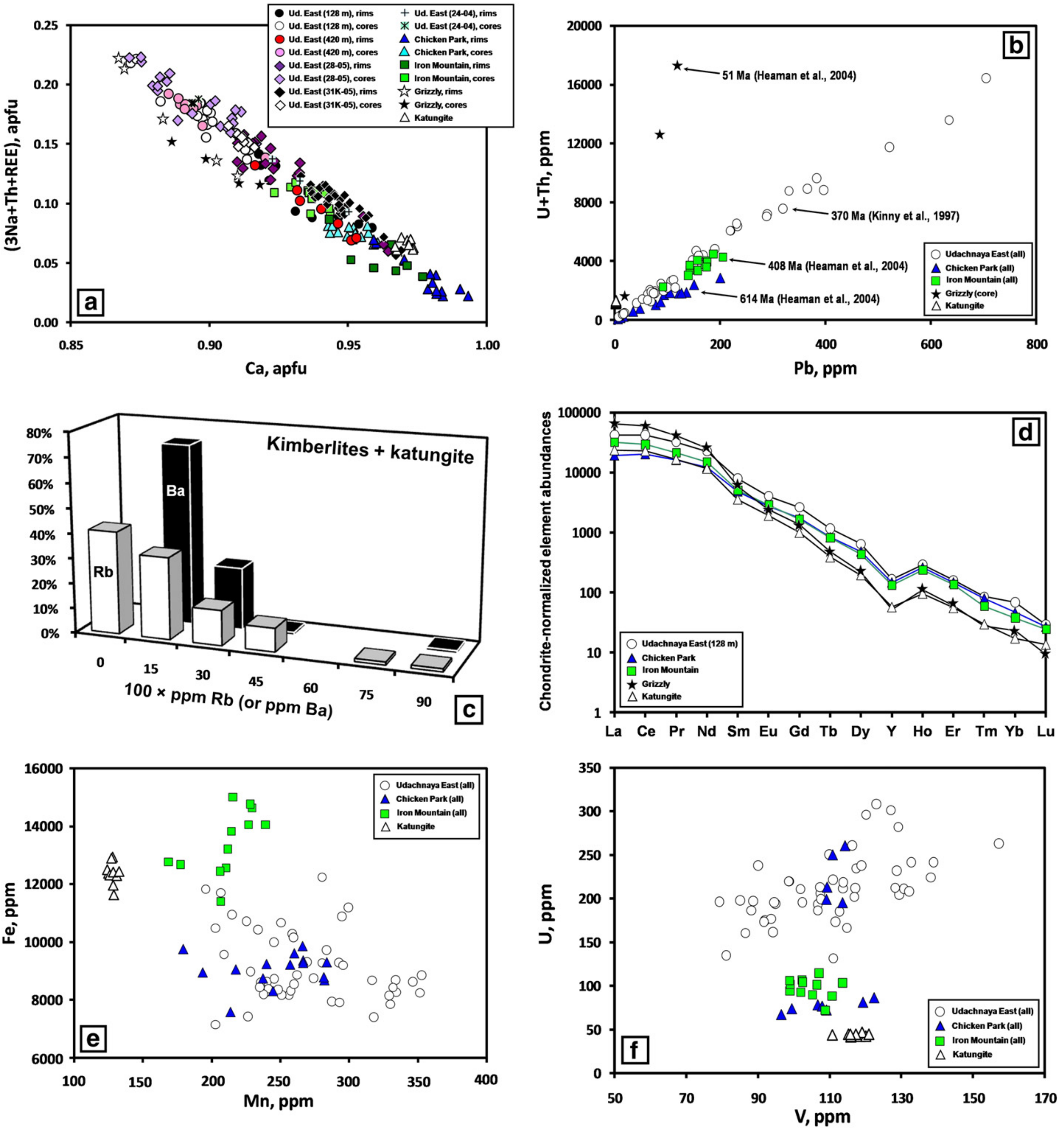

Fig. 3. Compositional variation of perovskite from kimberlites and katungite. (a) Correlation among the major cations substituting in the Ca site expressed in atoms per formula unit (apfu) calculated from the WDS data; (b) concentrations of Pb and actinides (in ppm) in perovskite of different age; (c) histograms of Rb and Ba distribution showing that the bulk of perovskite in kimberlites and katungite contains very low concentrations of these elements (cf. Melluso et al., 2008); (d) REE abundances (most REE-enriched perovskite compositions chosen for each locality) normalized to the chondrite values; (e-f) variations in the concentration of redox-sensitive elements.

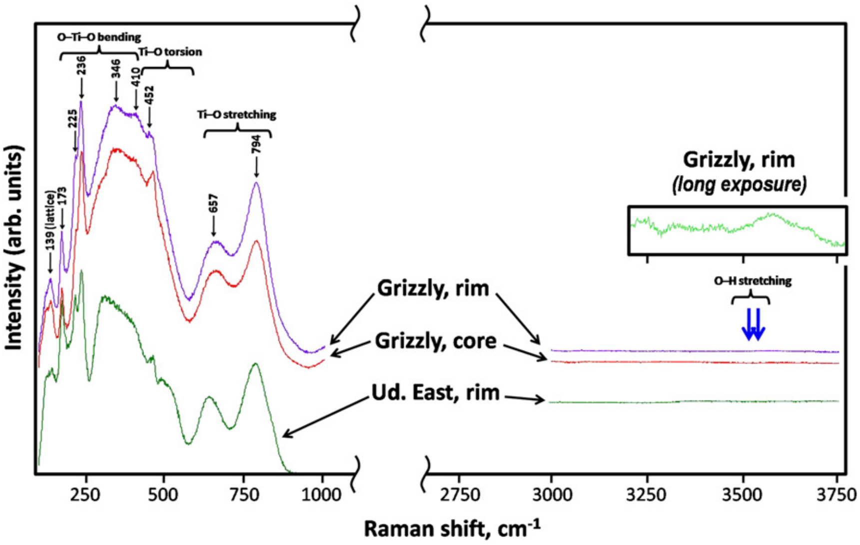

Fig. 4. Representative Raman spectra of perovskite showing characteristic lattice and Ti–O vibration modes and the absence of O – H modes near 3500–3550 cm^{-1}. The inset shows a long-exposure (2 min) spectrum showing the lack of any Raman scattering above the background level.

Lop, 2 mol% REEFeO$_3$ and 1 mol% Ltr; Table 1). It shows little variation in major- or trace-element composition; the subtle oscillatory zoning visible in BSE images (Fig. 2h) arises from minor variations in Fe and REE contents (1.3–1.7 and 3.0–3.6 wt% respective oxides).

The content of most trace elements (with the exception of Mn, Sr and V) varies by one order of magnitude or more within the entire dataset; the greatest variation (over three orders of magnitude) is observed for Th (Table 2). There is a distinct positive correlation between the Th + U and Pb values (Fig. 3b); individual samples define linear trends with a slope steepening from the Chicken Park array to the much younger Grizzly perovskite (614 and 51 Ma, respectively: Heaman et al., 2004). These systematic variations clearly indicate that a significant proportion of the measured Pb content is radiogenic. Of particular note are the consistently low Rb and Ba levels; none of the samples contain more than 1.25 ppm Rb or 80 ppm Ba, whereas 98% of all measured values are <0.8 ppm Rb and <25 ppm Ba (Fig. 3c). Although it may be argued that in the examined perovskite, Rb is hosted in submicroscopic inclusions of unknown minerals, Rb-bearing perovskites with an assortment of elements found in natural compositions can be readily synthesized (e.g., Gopalakrishnan et al., 1993) and, hence, there are no a priori reasons for dismissing the measured Rb values as contamination. The Cs content is consistently below its limit of detection by LA-ICP-MS (~0.2 ppm), obviously due to the 50%-larger ionic radius of Cs in comparison with Ca (Shannon, 1976).

The REE budget of all examined perovskite samples is dominated by Ce and other light REE [La ≥ Nd > Pr > Sm; $(La/Yb)_{CN} = 245–3673$ in the kimberlites and 1216 ± 88 in the katungite]. Chondrite-normalized REE distribution patterns are smooth, but show a prominent negative Y anomaly, reflecting a strongly subchondritic Y/Ho ratio (Fig. 3d; see below). The measured variation in Mn, Sr and V is less significant (110–350, 1150–2020 and 80–160 ppm, respectively); the katungite sample has Mn and V values comparable to those in the kimberlitic perovskite, but higher levels of Sr (3340–3580 ppm). None of the transition elements whose partitioning behavior is sensitive to redox conditions (V, Mn, Fe and U) exhibit a coherent variation among or within the samples (Fig. 3e and f). The Th/U ratio ranges from <0.1 (peripheral areas in some of the Udachnaya East perovskite) to 213 (Grizzly), whereas the Nb/Ta ratio is consistently near- to subchondritic (3.2–19.8). The Y/Ho and Zr/Hf values are invariably subchondritic, show little variation, and are essentially identical in the kimberlites and katungite (Y/Ho = 16.4 ± 1.5 and 16.9 ± 0.4; Zr/Hf = 18.7 ± 1.8 and 20.2 ± 0.5, respectively).

Several Raman measurements were made for each of the samples (including core and rim areas in the same crystal). All perovskite crystals produce well-defined and essentially identical micro-Raman spectra (Fig. 4) containing a lattice vibration at ~140 cm^{-1} and several intense signals associated with various Ti – O modes in the 170–800 cm^{-1} range (Moreira et al., 2009; Pontes et al., 2009). Raman spectroscopy is sensitive even to trace amounts of hydrogen trapped at defects in the perovskite lattice (Klauer and Wöhlecke, 1994), but none of the spectra obtained in the present work exhibit O – H stretching vibrations in the 3500–3600 cm^{-1} range. Long-exposure measurements (>1 min) in that wavenumber range also failed to detect any Raman signal above the background noise, effectively ruling out the presence of $(OH)^-$ groups (Fig. 4).

3.3. Zoning in perovskite from kimberlites

The Chicken Park, Iron Mountain and Udachnaya East samples contain relatively minor levels of substituent elements; their core is consistently enriched in Na, rare-earth elements (REE), Th and Ta; the maximum levels of these elements are observed in the Udachnaya East material (up to 1.1 wt.% Na_2O, 7.4 wt.% REE_2O_3, 2.7 wt.% ThO_2 and 0.6 wt.% Ta_2O_5). These samples show good positive correlations among the aforementioned elements, with their core areas plotting toward the top of each correlation trend (Fig. 5a–c). None of the other elements, including K and Sr (see Section 5.1), exhibit a consistent variation pattern among the studied kimberlites. For example, Al is typically concentrated in the core of the Udachnaya East perovskite, which is not observed in the rest of the samples (Fig. 5d). By contrast, the Chicken Park and Iron Mountain perovskite is characterized by a positive correlation between U and Th (and by extension, other elements enriched in the core; Fig. 5e). The Nb content either decreases or does not change significantly, whereas the Nb/Ta ratio invariably increases rim-ward. This trend is accompanied by a decrease in Th/U ratio toward progressively more Ta – Th-depleted compositions (Fig. 5f); the Zr/Hf and Y/Ho ratios do not show any systematic intragranular variation (see Section 3.2).

The core of perovskite crystals from Grizzly is similar to the most trace-element-enriched compositions from Udachnaya East (Figs. 3 and 5). However, their style of zoning is completely different in that it involves enrichment in Fe, Nb and Zr (up to 6.1, 16.6 and 1.0 wt.% respective oxides) in the euhedral high-AZ overgrowth (Fig. 5f) not accompanied by any significant change in Th, REE or Ta content. These compositions plot away from the main kimberlitic trend in the Na vs. REE diagram due to their low Na content for the given level of REE enrichment (Fig. 5a), indicating that a significant proportion of lanthanides is incorporated in this perovskite as the hypothetical REE(Fe,Al)O_3 components. Because of the narrow width of Fe–Nb-rich overgrowth (Fig. 2f), its trace-element composition could not be determined.

4. Geochemical considerations

4.1. Compositional variation of kimberlites and its petrogenetic implications

In order to be able to interpret the compositional variation of perovskite from a petrologic standpoint, we compiled an extensive database (211 entries) of whole-rock compositions of archetypal hypabyssal kimberlites based on the most recent (post-1998) literature and our own unpublished data for 75 intrusions from 22 kimberlite fields worldwide (Table 3). Where multiple analyses were available for a single intrusion, these were averaged to avoid overrepresentation of specific localities and fields. The complete list of localities and references are given in Appendix 3-I. For comparison, Table 3 also provides average whole-rock data for seven occurrences of katungite in Brazil and Uganda (Brod et al., 2005; Rosenthal et al., 2009). These data are further summarized as histograms and element-ratio variation diagrams in Fig. 6 and Appendix 3-II. The character of data distribution shows that the majority of kimberlites exhibit relatively little variation in their trace-element budget, especially given the geographical spread of the localities included in the present survey. The major-element, trace-element and ratio histograms (App. 3-II) do not show any convincing evidence of two or more distinct types of kimberlite magma (cf. Kjarsgaard et al., 2009). The data also tend to form a fairly tight cluster (*nota bene*, not two clusters) on the element-ratio diagrams (Fig. 6). The apparent "bimodality" of Ti distribution is echoed in the Fe pattern, but is not observed for Si, Mg, Ca and Al or other elements (cf. Figs. a–o in App. 3-II). A good positive correlation between the Fe and Ti contents (Fig. 7a) suggests that the data distribution shown here arises, to a great extent, from variations in the content of a single Fe–Ti oxide phase. The only two minerals that are reasonably common in kimberlites and could potentially cause the observed data scatter are macrocrystic or groundmass ilmenite [$(Fe^{2+},Mg,Fe^{3+})(Ti,Fe^{3+})O_3$] and groundmass spinel [$(Fe^{3+},Fe^{2+},Mg)_2(Fe^{2+},Ti)O_4$]. The latter contains a much smaller proportion of Ti relative to the total Fe content and will not produce the type of trend shown in Fig. 7a. Variations in the modal proportion of ilmenite and its Fe^{3+} content, on the other hand, can account for the concomitant enrichment of Fe and Ti in some kimberlites.

In addition to the lack of any evidence for bi- or multimodal distribution, most of the trace-element histograms show a conspicuous "train" tapering off toward higher element abundances in all cases with the exception of Ni (App. 3-II). This type of data distribution is consistent with crystal fractionation, where evolved rocks, which are most different from the parental magma in trace-element budget, would be much rarer than their less-evolved counterparts (App. 3-II). The whole-rock Ni content shows a reasonable positive correlation with the Mg and Co contents, and a negative correlation with the Co/Ni ratio (Fig. 7b and c). These variation trends are consistent with fractionation of Mg-rich olivine, which has a much greater affinity for Ni than Co (i.e. ${}^{Ol/L}D_{Ni} > {}^{Ol/L}D_{Co}$: Dale and Henderson, 1972; Leeman and Scheidegger, 1977; Adam and Green, 2006; Herd et al., 2009). The entire range of kimberlite compositions from ~2700 ppm to 350 ppm Ni and from Co/Ni = 0.04 to 0.18 can be accounted for by fractionation of 20 wt.% olivine (F_{Ol}) with ${}^{Ol/L}D_{Ni} \approx 10$ and ${}^{Ol/L}D_{Co} = 3$, where the majority of the data are bracketed by $F_{Ol} = 10$ and 15 wt.% (Fig. 7c). Our calculated partition coefficients are well within the range of values reported in the literature for basic and ultrabasic melts (see references above). It has been established experimentally that olivine is a ubiquitous early-crystallizing phase in kimberlitic melts (e.g., Edgar and Charbonneau, 1993; Mitchell, 2004). No claim is made here that the observed data patterns result exclusively from crystallization processes in kimberlitic magma; voluminous contributions of olivine from a variety of mantle sources should not be neglected and potentially account for the bulk of olivine in some kimberlites (e.g., Arndt et al., 2010). The main purpose of the above calculations and their relevance to the present work are in demonstrating that (1) crystal fractionation appears to play an important role in kimberlite petrogenesis, and (2) it can have a radical effect on the trace-element budget of kimberlite even at low percentages of fractionated crystals.

Whereas fractionation of olivine, spinel and possibly other ferromagnesian phases (e.g., Pasteris, 1983; Eccles et al., 2004; Tappe et al., 2012) is expected to cause depletion of evolved kimberlites in certain compatible trace elements, accompanied by their enrichment in Ba, Sr, Nb and other elements not readily incorporated in the early-crystallizing mineral assemblage (e.g., Fig. 6a and b), it does not explain significant spread in La/Yb and Th/U ratios (59–625 and 0.8–18.5, respectively), or "anomalous" Nb/Ta and Zr/Hf values in some kimberlites (Fig. 6c and d). It is feasible that the observed variations arise from fractionation of a phase or phases concentrating the rare-earth and high-field-strength elements (HFSE) and, hence, controlling the bulk of the incompatible trace-element budget of kimberlites. The potential effects of perovskite crystallization on kimberlite geochemistry will be examined below in Section 5.3.

4.2. Compositional variation of katungites and comparison with kimberlites

In common with kimberlites, katungites are enriched in Mg, Ca and incompatible elements, but relatively poor in Al (Table 3). The Mg content of the latter rocks is lower, whereas their Ca, Al, Fe and Ti levels are typically higher than in kimberlites (App. 3-II). The main compositional characteristics of katungites and other related members of the kamafugite clan have been addressed in detail elsewhere (Mitchell and Bell, 1976; Foley et al., 1987; Eby et al., 2003; Brod et al., 2005; Rosenthal et al., 2009) and will not be repeated here. The trace-element composition of katungites is compared to those of kimberlites and other undersaturated mantle-derived rocks in Figs. 6 and 8. From these diagrams, it is obvious that kimberlites are most similar to katungites in terms of their trace-element geochemistry and, in particular, REE and HFSE budget; this similarity has been previously recognized also by Mitchell and Bell (1976). Both rock types show strong enrichment in light lanthanides relative to Y and heavy lanthanides and in Nb + Ta relative to Zr and Hf, but their Y/Ho, Zr/Hf, Nb/Ta, Th/U and Ba/Nb ratios approach the primitive-mantle values (McDonough and Sun, 1995). Their normalized trace-element patterns are characterized by a steep negative REE slope and relative depletion in K, Rb, Cs, Sr, Pb and Zr + Hf in comparison with elements of similar compatibility (cf., for example,

Fig. 5. Compositional variation of perovskite from kimberlites and katungite. (a) Correlation between the Na and REE contents (apfu); (b) correlation between the REE and Th contents (ppm) in zoned perovskite from kimberlites (in each dataset, Th-depleted compositions are at the rim); (c) correlation between the Ta and Th contents (ppm) in normally zoned perovskite from the Udachnaya East, Chicken Park and Iron Mountain kimberlites (Fig. 1d–f); (d) positive correlation between the REE and Al contents (ppm) in the Udachnaya East perovskite; (e) positive correlation between the U and Th contents in the Chicken Park and Iron Mountain perovskite (the Udachnaya East compositions do not show any correlation and plot outside this range); (f) correlation between the Nb and Fe contents (apfu) in zoned perovskite from Grizzly (see Fig. 1 g); (g) correlation between the Nb/Ta and Th/U ratios in normally zoned perovskite arising from the different compatibilities of the elements in each of the pairs.

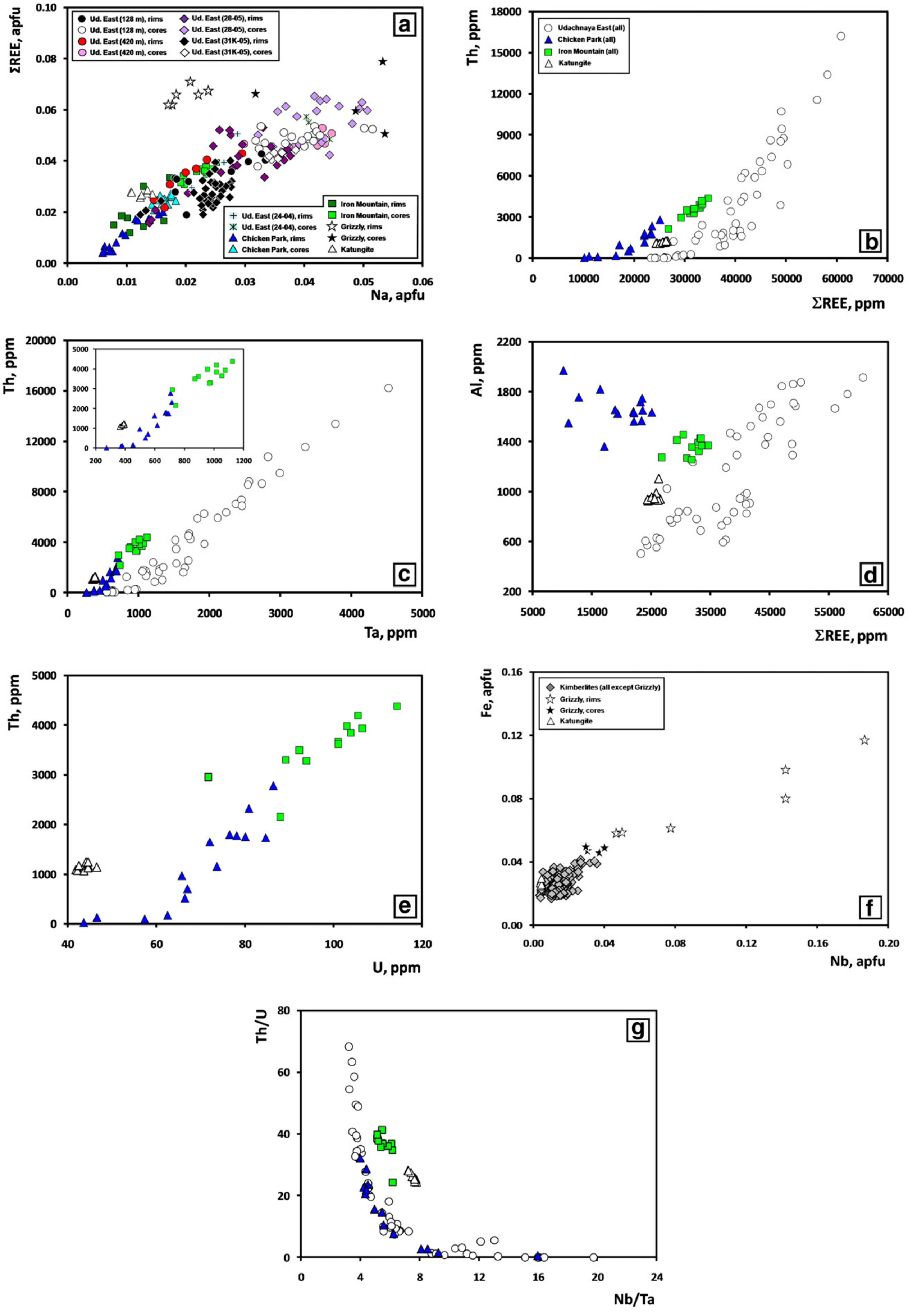
a
ΣREE, apfu
Na, apfu
Ud. East (128 m), rims
Ud. East (128 m), cores
Ud. East (420 m), rims
Ud. East (420 m), cores
Ud. East (28-05), rims
Ud. East (28-05), cores
Ud. East (31K-05), rims
Ud. East (31K-05), cores
Ud. East (24-04), rims
Ud. East (24-04), cores
Chicken Park, rims
Chicken Park, cores
Iron Mountain, rims
Iron Mountain, cores
Grizzly, rims
Grizzly, cores
Katungite
b
Th, ppm
ΣREE, ppm
Udachnaya East (all)
Chicken Park (all)
Iron Mountain (all)
Katungite
c
Th, ppm
Ta, ppm
d
Al, ppm
ΣREE, ppm
e
Th, ppm
U, ppm
f
Fe, apfu
Nb, apfu
Kimberlites (all except Grizzly)
Grizzly, rims
Grizzly, cores
Katungite
g
Th/U
Nb/Ta

Table 3
Whole-rock geochemistry of kimberlites and katungites.

Kimberlites[a]	Mean	ESD	Range	Katungites[b] mean	ESD	Range
Oxide, wt.%						
SiO_2	31.6	4.6	12.7–42.2	36.3	3.5	31.80–40.90
TiO_2	1.8	1.2	0–5.4	4.5	0.7	3.75–5.93
Al_2O_3	3.0	1.3	0.2–8.8	6.5	0.8	5.62–7.96
MgO	28.3	5.6	8.0–44.9	13.4	2.2	9.34–17.29
CaO	9.5	4.6	0.8–29.3	13.0	3.0	8.43–16.56
MnO	0.17	0.04	0.05–0.38	0.20	0.03	0.14–0.22
FeO_{Σ}	8.7	1.9	3.1–14.8	10.8	1.9	8.36–14.42
Na_2O	0.2	0.2	0–1.2	1.2	0.6	0.32–2.43
K_2O	0.9	0.6	0.1–3.3	3.4	1.2	2.12–5.98
P_2O_5	0.8	0.7	0–4.2	1.0	0.2	0.58–1.29
Element, ppm						
Sc	15	5	1.2–31	20	8	10–31
V	117	65	17–354	217	123	95–447
Cr	1371	468	611–3489	579	243	64–846
Co	80	15	24–135	51	8	39–60
Ni	1130	336	351–2641	262	145	68–504
Ga	4.9	2.0	0.1–11.0	13.6	1.6	12.0–16.0
Rb	64	42	1.1–245.0	89	32	43–121
Sr	854	416	124–2368	2194	575	1221–2742
Y	14	10	0.7–68	19	4	13–29
Zr	202	257	5–2078	378	107	272–580
Nb	181	72	23–417	234	72	126–354
Cs	2.0	2.6	0–16.9	0.7	0.4	0.2–1.3
Ba	1535	850	77–7274	1885	423	898–2238
La	138	63	13–336	195	64	100–276
Ce	251	120	25–701	358	122	203–513
Pr	26	12	2.3–80	46	13	32–65
Nd	89	47	6.9–299	152	36	95–185
Sm	12	6	0.8–42	20	3	15–23
Eu	3.0	1.7	0.2–10.7	5.0	1.1	3.7–6.8
Gd	8.6	4.9	0.6–25.0	39	10	21–46
Tb	0.8	0.5	0–2.8	11.3	2.1	8.4–14.0
Dy	3.6	2.0	0.2–12.6	4.9	1.0	3.5–6.8
Ho	0.5	0.3	0–1.9	0.7	0.1	0.5–1.0
Er	1.2	0.6	0.1–3.7	1.5	0.3	1.1–2.2
Tm	0.15	0.09	0–0.6	0.19	0.03	0.14–0.23
Yb	0.8	0.4	0.1–2.2	1.1	0.2	0.8–1.6
Lu	0.11	0.06	0–0.4	0.17	0.01	0.15–0.21
Hf	4.5	5.2	0.2–41	8.5	2.0	6.2–12.4
Ta	10.2	3.9	1.8–22.9	13.2	3.5	9.0–19.0
Pb	10.1	7.8	0.7–80.0	9.3	1.9	6.9–12.0
Th	19	9	4–52	21	7	12–34
U	4.2	2.8	1.0–40.4	5.4	1.9	2.9–8.0

	Kimberlites[a] mean	ESD	Katungites[b] mean	ESD
Selected element ratios (mass)[c]				
Sc/Mg	1.0×10^{-4}	0.5×10^{-4}	2.4×10^{-4}	0.9×10^{-4}
Co/Ni	0.074	0.020	0.29	0.18
Co/Mg	4.6×10^{-4}	0.9×10^{-4}	6.6×10^{-4}	0.4×10^{-4}
V/Cr	0.098	0.067	0.65	0.78
Ga/Al	3.9×10^{-4}	1.1×10^{-4}	4.1×10^{-4}	0.9×10^{-4}
Rb/K	9.3×10^{-3}	4.6×10^{-3}	3.5×10^{-3}	0.9×10^{-3}
Rb/Ba	0.048	0.028	0.048	0.009
Y/Ho	26	3	27	2
La/Yb	211	123	175	53
La/Nd	1.7	0.5	1.3	0.2
Ba/Sr	2.1	1.7	0.8	0.1
Ba/La	11.9	5.8	10.0	1.9
Ba/Nb	8.9	4.9	8.3	1.4
Zr/Hf	42	7	44	4
Zr/Nb	1.2	1.0	1.7	0.7
Nb/Ta	17.7	4.7	17.7	2.0
Nb/Th	10.1	3.7	11.4	3.2
Th/U	5.0	1.8	4.0	0.9

[a] Calculated for a reduced dataset (77 entries) based on 211 whole-rock analyses of 75 kimberlite bodies from 22 kimberlite fields (see Appendix 3 for locality names, references and element histograms).

[b] Calculated for a reduced dataset (7 entries) based on 10 whole-rock analyses of katungite from Uganda (Tappe et al., 2003; Rosenthal et al., 2009; A. Gurenko, pers. commun.) and Brazil (Brod et al., 2005).

[c] The mean values and estimated standard deviations (ESD) were calculated on the basis of the reduced dataset, not from the mean element abundances.

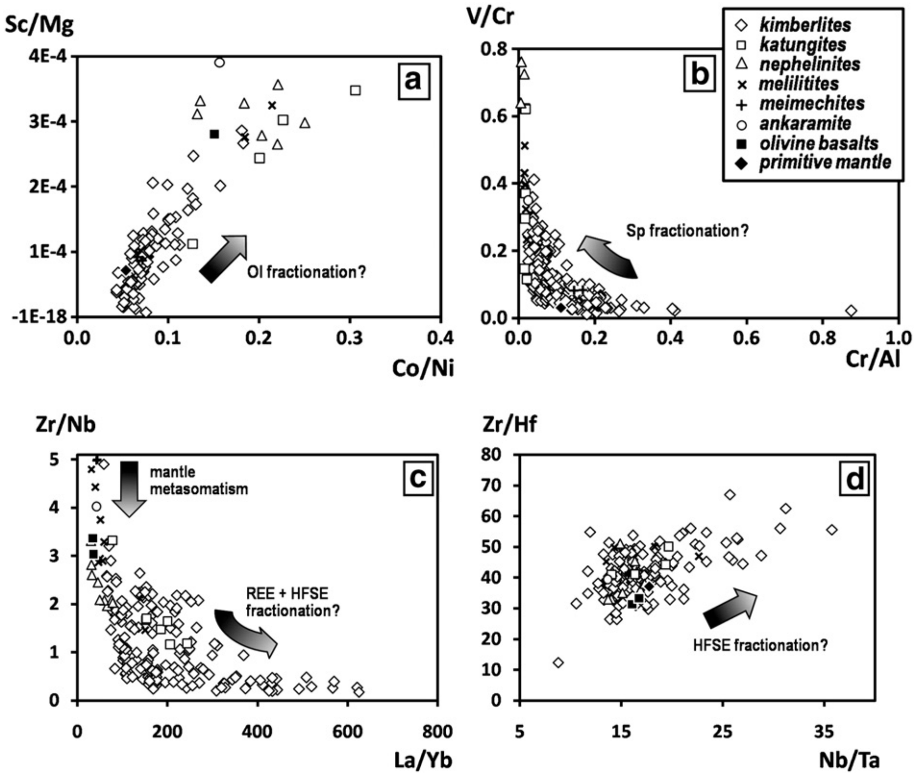

Fig. 6. Compositional variation of kimberlites (see Appendix 3 for data sources) expressed in terms of selected element ratios and compared to the published compositions of the primitive mantle (McDonough and Sun, 1995) and primitive mantle-derived rocks (Upton et al., 1992; Hoernle and Schmincke, 1993; Arzamastsev et al., 2001; Janney et al., 2002; Ulrych et al., 2003; Brod et al., 2005; Keller et al., 2006; Rosenthal et al., 2009; Sobolev et al., 2009). Arrows indicate some possible evolutionary paths arising from fractionation of olivine and REE-HFSE phases.

Rb/Ba = 0.05 in kimberlites or katungites, and 0.09 in the primitive mantle). Thus, it is reasonable to propose that katungites are the closest counterpart to kimberlites in rift systems, even in comparison with melilitites and other rocks traditionally regarded as geochemically akin to kimberlites (e.g., Janney et al., 2002; Sobolev et al., 2009). Note that this similarity *does not necessarily imply a common origin* (this aspect of kimberlite petrogenesis is beyond the scope of the present study); it does, however, imply that kimberlitic and katungitic melts may serve as suitable analogues for estimating the effects of perovskite crystallization on the melt composition (see below).

5. Discussion and conclusions

5.1. Perovskite zoning: origin and relation to element partitioning

The type of zoning observed in the Chicken Park, Iron Mountain and Udachnaya East perovskite (see Sections 3.1 and 3.3) is very common in kimberlites (Chakhmouradian and Mitchell, 2000; Eccles et al., 2004; Ogilvie-Harris et al., 2009; Yang et al., 2009). It has probably gone unnoticed in many other cases because variations in trace-element levels are typically too subtle to be detected during a routine examination of BSE images. None of the other groundmass phases crystallizing simultaneously or prior to perovskite (e.g., olivine, monticellite or spinels) have the same structural capacity, and hence would be capable of competing with perovskite, for the trace elements defining this zoning pattern (i.e., Na, light REE, Th and Ta). Groundmass apatite can incorporate significant levels of Na and REE (Chakhmouradian and Mitchell, 1999; Chakhmouradian et al., 2002), but in our samples, this mineral postdates perovskite.

If the growth of perovskite outpaced the rate of its chemical re-equilibration with the host melt, sequestration of the most compatible elements by this mineral led to their progressive depletion in the melt proportionally to the mass fraction of crystallized perovskite (F_{Prv}) and perovskite-melt partition coefficient (D_X). It is thus feasible that the drastic rim-ward decrease in the content of these elements (Fig. 5a–c) stems from their extremely high compatibility with respect to the perovskite structure, i.e. model (1); the effects of element partitioning on zoning have been discussed in detail by Reguir et al. (2008).

Alternatively, the observed pattern could arise from:

(2) Changes in element partitioning (e.g., a decrease in D_{Th} and D_{Ta}) owing to depressurization and release of volatiles during the emplacement of kimberilte;
(3) Changes in the availability of certain elements owing to their partial loss into a fluid phase;
(4) Postemplacement re-equilibration of perovskite with the host kimberlite (± fluid) via solid-state diffusion.

The four mechanisms are further compared in Fig. 9. Model (2) implies that elements such as REE, Th and Ta become much less compatible (by up to an order of magnitude) in a devolatilized kimberlite melt, whereas model (3) requires a substantial loss of these elements into a fluid phase not accompanied by any significant changes in D_X. Neither of these interpretations is consistent with the lack of any textural or mineralogical evidence of fluid release in the examined kimberlites (cf. Skinner and Marsh, 2004), nor with the apparently gradual core-rim transition in the zoned perovskite crystals (Fig. 1c–f). Although theoretical considerations indicate that high levels of H_2O in the melt suppress partitioning of trace elements into a solid phase (Wood and Blundy, 2002), the actual changes in D_X values of specific elements are difficult to predict (e.g., Gaetani et al., 2003). The effect of volatile content on trace-element partitioning in $CaTiO_3$ is unknown, but $CaSiO_3$ perovskite shows no appreciable change in D_X in hydrous silicate melts relative to "dry" ones (Corgne et al., 2005). In basanitic systems, the elements depleted in the rim of perovskite crystals partition strongly into a silicate melt relative to a conjugate fluid (${}^{Fluid\text{-}L}D<0.1$: Adam et al., 1997). To summarize, the published experimental evidence does

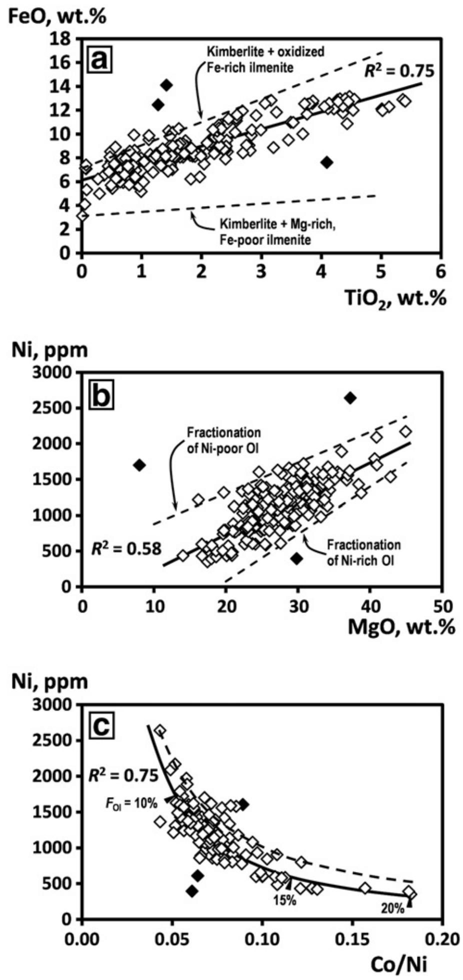

Fig. 7. Selected variation diagrams for kimberlites (see Appendix 3 for data sources); each correlation trend and R^2 value was calculated after the subtraction of three outliers departing the farthest from the trend (solid diamonds). (a) Positive correlation between the TiO_2 and FeO contents in kimberlites that can be explained by the presence of variable amounts of ilmenite macrocrysts; the dashed lines indicate the limits of this variation dependent on the Fe/Ti proportion in oxidized and unoxidized ilmenite (calculated from the data of Pasteris, 1980; Wyatt et al., 2004 and Robles-Cruz et al., 2009). (b) Correlation between the MgO and Ni contents in kimberlites that can be explained by olivine fractionation; variations in Ni content of the fractionating olivine can generate any trend within the area delineated by dashed curves (olivine data after Kamenetsky et al., 2008). (c) Correlation between the Co/Ni ratio and Ni content of kimberlites showing a model fractionation curve based on the experimental data for basanite (dashed curve; $D_{Ni} = 32$ and $D_{Co} = 4$ from Adam and Green, 2006); the entire correlation trend (solid curve) can be modeled by reducing the partition coefficients to $D_{Ni} = 10.2$ and $D_{Co} = 3$. Note that Ni correlates positively with Co ($R^2 = 0.60$, not shown), further supporting olivine fractionation.

not provide any support for models (2) and (3) because devolatilization of kimberlitic magma is expected to either have little compositional effect on the crystallizing perovskite, or enhance partitioning of REE, Th and Ta into this mineral.

Subsolidus re-equilibration, i.e. our model (4), would produce a diffuse core-rim boundary, whose distance from the edge would vary depending on the kinetics of diffusion and the presence or absence of passageways (defects, fractures, etc.) facilitating element transport across the crystal-matrix interface. In our case, the core-rim boundary is diffuse, but crystallographically defined, and does not appear to correlate with peripheral fracturing in perovskite crystals (e.g., Fig. 1c). More importantly, REE^{3+} and Th^{4+} are more strongly bonded to oxygen in the perovskite structure than mono- or divalent cations substituting for Ca. Bond-valence values (BV), calculated on the basis of the average cation-oxygen distance of 2.727 Å using the formalism of Brown and Altermatt (1985), are >0.2 for REE^{3+} and Th^{4+} and <0.2 for Na^+, K^+ and Sr^{2+}. Intuitively, the rate of diffusion must be appreciably faster for the latter cations, which is in accord with compositional variations recognized in cation-leached perovskites by Chakhmouradian et al. (1999). Tantalum forms even stronger bonds to oxygen (1.956 Å, BV≈0.91) and is virtually unsusceptible to chemical re-equilibration. Hence, the rim-ward decrease in REE, Th and Ta, not accompanied by any systematic changes in K or Sr content, cannot be feasibly explained by model (4).

On the basis of the evidence presented above, we conclude that the common occurrence of the type of zoning shown in Fig. 2c–e (termed “normal zoning” by Chakhmouradian and Mitchell, 2000) in different kimberlite facies is underpinned by crystal-chemical controls of element partitioning.

The Grizzly material shows a very different pattern of zoning (Fig. 2f) that cannot be satisfactorily explained by the above mechanisms. Compositionally and morphologically similar perovskite enriched in Na, REE, Nb and Fe has been described from hypabyssal and crater-facies kimberlites on the Diavik mine property, also in the Lac de Gras kimberlite field, by Chakhmouradian and Mitchell (2001), who hypothesized that this unusual zoning formed by reaction of the earlier-crystallized perovskite with a melt enriched in incompatible elements. This interpretation is consistent with the spectroscopic data presented in Section 3.2. Because Raman-detectable protonation of perovskite can be achieved at relatively low $P(H_2O)$ levels (~0.4 kbar: Klauer and Wöhlecke, 1994), the absence of O–H modes in the spectra of the late-stage overgrowth (Fig. 4) argues against the involvement of a hydrous fluid in its formation. The existence of an evolved kimberlitic melt at Grizzly and other Lac de Gras localities has also been suggested by Armstrong et al. (2004), although its exact origin has not been addressed. It is feasible that early loss of fluid from the kimberlite magma at Grizzly, postulated by Fedortchouk and Zhang (2011) on the basis of microdiamond morphology, led to concentration of fluid-incompatible elements in the melt, enabling zoning mechanism (3) (see above).

5.2. Element partitioning in perovskite

For the calculation of perovskite-groundmass partition coefficients, we chose four samples of aphanitic or macrocryst-poor kimberlite (one from each Chicken Park and Iron Mountain, plus two from Udachnaya East) and the Bunyaruguru katungite. The chosen samples are fine-grained and uniform in texture (Fig. 1). The calculations were straightforward for the Bunyaruguru perovskite because it shows little compositional variation (Figs. 3 and 5) and its host vitrophyric rock is probably representative of the parental katungitic magma (Table 4). In the four kimberlite samples, the groundmass may or may not approach in composition the kimberlitic melt at the time of perovskite crystallization, and the compositional variations within perovskite crystals had to be accounted for. Consequently, we performed two series of calculations. In the first series (Table 4), the average perovskite composition in each of the samples was assumed to be in equilibrium with its host groundmass, and the groundmass was assumed to represent the parental kimberlitic magma within the uncertainty limits established above for the global kimberlite dataset (Section 4.2). The standard deviations in partition coefficients were determined by error propagation (Table 4) and effectively account for potential deviation of the groundmass composition from that of the *real* kimberlitic magma.

In the second series of calculations, we assumed that perovskite growth outpaced the rate of its re-equilibration with the magma (assumed to be compositionally equivalent to the groundmass) and calculated changes in element concentrations in the fractionating perovskite (C_{Prv}) using the following equation:

$$C_{Prv} = \left[C_o - C_o{}'(1-F_{Prv})^{DX}\right]/F_{Prv},$$

where C_o is the concentration of element X in the groundmass, F_{Prv} is the proportion of fractionated perovskite (F_{Prv}) by mass, and D_X is the

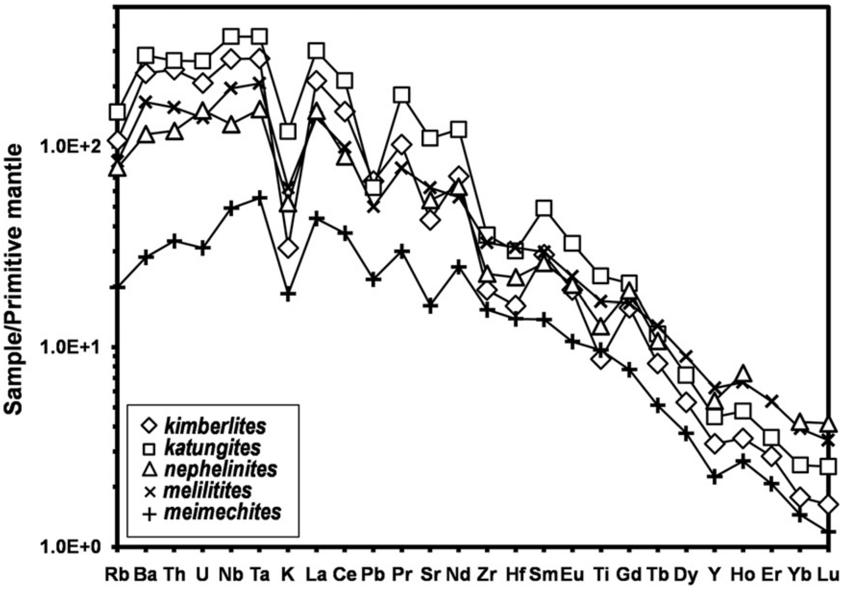

Fig. 8. Average composition of kimberlites (Table 3) and other mantle-derived rocks normalized to the primitive mantle of McDonough and Sun (1995). The katungite composition is an average of 10 whole-rock analyses (Brod et al., 2005; Tappe et al., 2009; this work); the nephelinite and melilitite patterns were calculated for rift occurrences only (8 and 14 analyses, respectively, from Wilson et al., 1995; Arzamastsev et al., 2001; Janney et al., 2002; Ulrych et al., 2003; Keller et al., 2006), and the meimechite composition is an average of four analyses from Sobolev et al., 2009).

perovskite-melt partition coefficient for element X. The F_{Prv} values were determined from the relative volume occupied by the high-AZ core and low-AZ rim of perovskite crystals. Because a significant proportion of Pb in all kimberlite samples is radiogenic (Fig. 3b), their C_o values for Pb, U and Th were recalculated to take into account radioactive decay using the previously determined radiometric ages (Kinny et al., 1997; Heaman et al., 2004). The D_X values were computed by iteration, i.e. step-wise modeling of simultaneous changes in the composition of the melt and fractionating crystals to bring the calculated element concentrations (C_{Prv}) as close as possible to those determined analytically by WDS and LA-ICP-MS. For most of the elements (ca. 90% of all data), deviation of the calculated C_{Prv} value from the measured one was less than 10%, and only in a few cases, did the fractional error exceed 30% (Pb and Hf in sample Udachnaya East-128 m; Na, Rb and Zn in Udachnaya East-420 m). The two sets of partition coefficients (Tables 4 and 5) compare reasonably well, but the propagated errors listed in the first set are certainly a more realistic reflection of the uncertainties associated with this type of empirically derived data.

With the exception of Na, Pb and Zr, the calculated D_X values are remarkably consistent between the average kimberlite and katungite datasets (Table 4; Figs. 10a and b). The remaining elements can be somewhat arbitrarily grouped into strongly incompatible ($D_X \ll 0.1$: K, Rb, Zn, Ba, Al), moderately incompatible ($D_X = 0.1$–0.5: Mn, Ga, Sc, V, Fe), compatible ($D_X = 1.0$–5.0: Ca, Sr, Hf, heavy REE), and strongly compatible ($D_X > 5.0$: Y, light- to mid-range REE, Th, U, Ti, Nb, Ta). Sodium and Zr appear to be less compatible in katungite ($D_X = 0.2$ and 0.5, respectively) relative to kimberlites (0.8–11 and 1.1–1.6, respectively). Note, however, that the wide range of D_{Na} values in the latter may indicate loss of Na from the kimberlitic magma during its emplacement, resulting in low Na levels in the groundmass and, consequently, overestimated partition coefficients. The low partition coefficient obtained for Na in the katungite sample (0.19) is probably more realistic and agrees with a value of 0.17 obtained by Onuma et al. (1981) for perovskite from the Nyiragongo nephelinite. The D_{Pb} coefficient is much higher in the kimberlites (5–14) relative to the katungite (0.3), even after corrections for U–Th decay (see above). Note that in the Onuma diagram for the katungite sample, the D_{Pb} value fits the empirical curve for divalent cations, plotting between the partition coefficients for the smaller Sr^{2+} and larger Ba^{2+} (Fig. 10b), which is not the case for any of the kimberlite samples or the average kimberlite D_{Pb} value, falling significantly off the Sr–Ba trend (extrapolated $D_{Pb} \approx 0.9$; Fig. 10a). Because there is no evidence for Pb loss during, or subsequent to, the emplacement of kimberlitic magma (e.g., Smith et al., 2004), the only plausible explanation for the above discrepancy is that the actual amount of common Pb in perovskite is much lower than that calculated on the basis of the radiometric age and current concentrations of U and Th in this mineral. For example, in the Iron Mountain perovskite, the initial Pb content of ca. 5 ppm (as opposed to the age-corrected value of 71 ppm) would give the D_{Pb} coefficient of 0.9. This interpretation would have serious implications

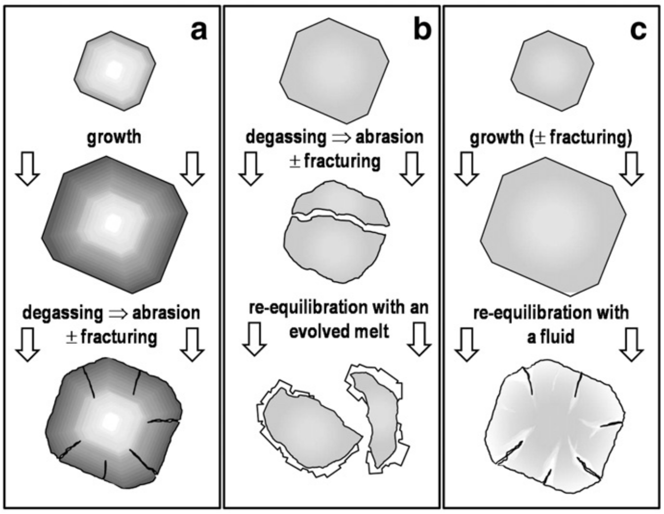

Fig. 9. Schematic diagram showing the effects of different element compatibility (a), magma devolatilization (b) and subsolidus processes (c) on perovskite zoning. (a) The most common type of zoning in kimberlitic perovskite (cf. Fig. 1d–f) corresponding to model (1) discussed in Section 5.1; (b) discontinuous zoning arising from degassing and enrichment of the residual melt in fluid-incompatible elements, such as Nb (cf. Fig. 1g); (c) subsolidus re-equilibration of perovskite with a fluid resulting in selective removal of weakly-bonded cations (e.g., Na^{+}, Ca^{2+} and Sr^{2+}); this type of zoning probably occurs in perovskite from the Mengyin kimberlite, China (cf. Fig. 2f–k in Yang et al., 2009) and is fairly common in perovskite-group minerals from other rock types (e.g., Chakhmouradian et al., 1999).

for geochronology because it implies that the common-Pb content cannot be determined correctly without the precise data for individual isotopes (for further discussion, see Beyer et al., 2013–this volume).

Melluso et al. (2008) reported a similarly high average D_{Pb} for perovskite from Alto Paranaíba, Brazil (Fig. 10c), but their value is not age-corrected and is associated with a very large error (11 ± 16). Beyer et al. (2013–this volume) reported D_{Pb} ranging from 0.3 to 5 in silicate melts, i.e. overlapping the range of values determined in the present work. Unfortunately, none of the other publications on trace-element partitioning in synthetic and natural $CaTiO_3$ (Nagasawa et al., 1976; Onuma et al., 1981; Simon et al., 1994; Corgne and Wood, 2005) list Pb data. We recommend that the value obtained in the present work for the Bunyaruguru perovskite be used in modeling because it has not been affected much by U–Th decay and is in better accord with the partitioning data for other divalent cations.

Selected published partitioning data for synthetic and natural perovskites are shown in Fig. 10c. Our results for Sr, REE and Sc are in good agreement with the experimental data of Beyer et al. (2013–this volume) for a simulated kimberlite system; our values for HFSE are consistently higher than in the latter study, which may stem from a higher carbonate content in kimberlitic magmas relative to the experimental system (Beyer et al., 2013–this volume). With the exception of Sr, Al and Sc, the partition coefficients reported by Corgne and Wood (2005) are very different from those obtained in the present work. Whereas deviation of their HFSE coefficients to lower values relative to our data probably reflects the very different chemistry of their experimental system ($CaO + SiO_2 + TiO_2$) relative to any natural melt, the high D_K, D_{Rb} and D_{Ba} values reported by these authors are probably an artefact.

Apart from large differences in D_X across the lanthanide series, reported in all previously published studies, perovskite is characterized by higher partition coefficients for Ho in comparison with Y (Table 4). Analysis of the literature data obtained with different instrumentation (Melluso et al., 2008; Yang et al., 2009; Sarkar et al., 2011) confirms that the Y/Ho ratio in perovskite is consistently subchondritic and mostly falls in the 16.0–17.5 range (cf. Section 3.2). Owing to the lanthanide contraction, these two elements have essentially identical ionic radii (Shannon, 1976), and do not readily separate in the geological environment. Yttrium–Ho decoupling has been traditionally believed to be restricted to low-T aqueous processes (e.g., Bau, 1996) and, to our knowledge, has not been previously recognized in igneous systems. The

Table 4
Perovskite-groundmass partitioning data for kimberlites and katungite.

Kimberlites:	Chicken Park		Iron Mountain		Udachnaya East 128 m		Udachnaya East 420 m		Average kimberlite		Katungite, Bunyaruguru	
	D	σ_D[c]	D	σ_D[c]	D	σ_D[c]	D	σ_D[c]	$\overline{D}$	$\sigma_{\overline{D}}$[d]	D	σ_D[c]
Ca site:												
Na[a]	5.8	23.5	11	54	2.8	2.2	0.81	0.35	5.1	14.7	0.19	0.08
K	0.009	0.003	0.012	0.005	0.006	0.003	0.0089	0.0024	0.009	0.002	0.007	0.003
Rb	0.0005	0.0006	0.0005	0.0010	0.0008	0.0006	0.0013	0.0015	0.0008	0.0005	0.002	0.003
Ca[a]	4.5	2.4	5.0	3.0	3.2	1.3	4.0	2.0	4.2	1.1	2.5	0.5
Mn	0.17	0.04	0.12	0.03	0.060	0.008	0.055	0.006	0.10	0.01	0.077	0.011
Zn	0.020	0.014	0.025	0.025	0.013	0.012	0.017	0.016	0.019	0.009	0.022	0.009
Sr	1.29	0.51	2.6	1.6	0.56	0.10	0.57	0.10	1.26	0.42	1.26	0.26
Ba	0.007	0.005	0.017	0.019	0.0022	0.0008	0.0025	0.0011	0.007	0.005	0.008	0.002
Pb	5.7	5.5	13.7	18.9	5.0	3.7	6.6	4.2	7.8	5.1	0.33	0.08
Y	12.9	7.7	7.1	2.5	7.6	2.7	7.5	2.4	8.8	2.2	5.6	1.3
La	43.0	27.0	26.0	5.4	28.8	7.1	29.6	6.7	31.8	7.3	27.9	6.5
Ce	51.9	29.0	32.8	6.9	36.9	9.6	39.6	9.2	40.3	8.2	45.9	11.1
Pr	62.8	35.9	41.4	9.6	45.7	12.8	47.7	11.7	49.4	10.2	46.9	11.4
Nd	65.5	39.9	44.8	12.1	48.0	14.7	52.2	14.4	52.6	11.6	51.1	10.1
Sm	57.8	31.0	36.5	9.7	41.7	12.4	42.0	11.1	44.5	9.1	32.9	4.3
Eu	49.3	28.9	27.0	7.4	29.4	8.7	30.9	8.6	34.2	8.1	24.3	4.6
Gd	40.3	25.1	22.6	7.2	26.9	9.3	26.1	8.0	29.0	7.2	22.3	20.0
Tb	28.5	14.6	15.6	4.3	18.8	5.8	18.5	5.2	20.4	4.3	12.9	21.1
Dy	28.0	14.1	14.5	4.0	16.5	4.8	15.5	3.9	18.6	4.0	10.5	2.0
Ho	21.1	10.2	12.5	3.7	12.9	4.0	12.9	3.6	14.8	3.0	8.5	1.2
Er	15.3	6.6	8.2	2.2	8.2	2.5	8.3	2.0	10.0	1.9	5.6	1.1
Tm	10.6	5.4	5.0	1.7	5.6	2.4	4.9	1.4	6.5	1.6	3.9	0.6
Yb	6.6	2.5	3.3	0.9	3.4	1.3	3.0	0.8	4.1	0.8	2.8	0.5
Lu	4.5	2.2	2.9	1.1	2.4	1.0	2.2	0.8	3.0	0.7	1.9	0.3
Th	102	69	152	35	155	97	249	122	164	44	155	34
U	14.5	7.1	14.4	5.2	21.5	7.1	21.6	6.8	18	3.3	6.6	1.8
Ti site:												
Al	0.09	0.03	0.067	0.023	0.036	0.011	0.026	0.009	0.055	0.010	0.029	0.004
Sc[b]	0.34	0.11	0.19	0.06	0.18	0.10	0.16	0.08	0.22	0.04	0.12	0.04
V	0.49	0.19	0.89	0.49	0.31	0.08	0.28	0.08	0.49	0.13	0.5	0.3
Fe	0.11	0.02	0.13	0.02	0.16	0.05	0.14	0.04	0.14	0.02	0.14	0.02
Ga	0.12	0.04	0.16	0.06	0.08	0.06	0.08	0.03	0.11	0.02	0.064	0.014
Ti[a]	16.1	5.5	15.5	4.8	13.6	4.0	15.0	4.8	15.0	2.4	15.4	2.5
Zr	1.3	1.4	1.1	1.2	1.6	1.1	1.6	1.1	1.4	0.6	0.50	0.17
Hf	2.5	2.1	2.0	1.6	3.4	2.4	3.4	1.9	2.8	1.0	1.0	0.3
Nb	15.5	5.9	14.4	3.2	16.1	3.5	17.6	3.7	15.9	2.1	12.4	3.3
Ta	54.5	18.3	63.2	13.6	110	42	92	30	80	14	36.8	6.8

[a] The partition coefficients for Na, Ca and Ti were calculated from WDS data and for the rest of the elements, from LA-ICP-MS data.

[b] The assignment of Sc to the Ti site is tentative; synthetic perovskites with Sc in both cation sites (e.g., $LaScO_3$ and $ScAlO_3$) are known.

[c] σ_D calculated by error propagation from the standard deviations (σ_{Prv}) of the mean element abundances in perovskite (C_{Prv}) and standard deviations (σ_{WR}) of the mean whole-rock abundances C_{WR}: $\sigma_D(X) = D_X \times \sqrt{[(\sigma_{Prv}/C_{Prv})^2 + (\sigma_{WR}/C_{WR})^2]}$ (see Section 5.2 for further details).

[d] $\sigma_{\overline{D}} = \sqrt{[0.0625 \times (\sigma_{D1}^2 + \sigma_{D2}^2 + \sigma_{D3}^2 + \sigma_{D4}^2)]}$.

differences in partitioning behavior between these two elements in aqueous systems have been addressed in terms of involvement of *f*- or *s*- electrons in REE–ligand bonding (i.e., greater covalency of Ho relative to Y) or stereochemical changes during the transition from a solute to a solid (Choppin, 2002; Tanaka et al., 2008). Greater strength of the Ho – O bond is in accord with higher melting points of Ho perovskites relative to their Y counterparts (e.g., Weber et al., 1969; Mizuno, 1979) and may, in principle, explain the preferential Ho-over-Y partitioning in natural perovskite. Because the Ho – O bond is marginally stronger than the Y – O bond, the attachment of a Ho^{3+} cation to a growing perovskite crystal is energetically more favorable (Hartman and Perdok, 1955), resulting in a proportionately higher rate of Ho incorporation in comparison with Y. Further trace-element studies of perovskite from different igneous rocks are required to confirm if the observed Y-Ho decoupling is controlled by structural parameters (as proposed here), or structure-independent parameters, such as crystallization conditions or the rate of crystal growth.

In contrast to other elements, the D_X values for the small trivalent cations incorporated in the Ti site do not form a clear partitioning curve in Fig. 10. The smaller-than-expected partition coefficients for Fe, Ga and Al probably arise from their preferential incorporation into groundmass spinels co-crystallizing with perovskite (Figs. 1, 2a–d). Another element that is compatible with respect to spinel is Zn, whereas the partition coefficients of V and Sc are sensitive to redox conditions and approach the values reported above for perovskite (Horn et al., 1994). Crystallization of spinel will have little effect on the partitioning of other trace elements between perovskite and kimberlitic magma because of the low to extremely low compatibility of HFSE, REE and larger cations in spinel (Horn et al., 1994; Nielsen et al., 1992). In some kimberlites, perovskite appears to have crystallized contemporaneously with apatite and phlogopite (e.g., Sarkar et al., 2011). Because these minerals are effective sinks for some incompatible elements (Ba in phlogopite and Sr + REE in apatite), competitive partitioning will certainly affect the trace-element budget and zoning of the perovskite.

5.3. Implications for magma evolution

Perovskite is abundant (but not ubiquitous) in kimberlites, locally making up as much as 20 vol.% of the groundmass (Yang et al., 2009). Perovskite fractionation has been suggested to contribute to the chemical diversification of kimberlitic and other undersaturated magmas (Peterson, 1989; Melluso et al., 2008; Sarkar et al., 2011), but no quantitative assessment of this potential contribution has been provided in any of the studies. As can be expected from the trace-element compositions (Section 3.2), perovskite has a greater structural affinity for light REE (with a peak at Nd) vs. heavy REE, Ho vs. Y, Ta vs. Nb, Hf vs. Zr, and Th vs. U. The overall low partition coefficients for Zr and Hf (≤3) imply that perovskite crystallization will only have a significant effect on the Zr – Hf budget of the parental magma at very high F_{Prv} levels, probably unattainable in natural systems (due to the limited availability of Ti). Thorium, U, Nb, Ta and the majority of lanthanides, on the other hand, are highly compatible in perovskite (≥10), suggesting that the REE and HFSE geochemistry of undersaturated melts will be profoundly affected by perovskite fractionation even at low F_{Prv} values. To illustrate these effects, we calculated the composition of kimberlitic and katungitic melts undergoing fractionation of perovskite; the principal results are summarized in Fig. 11. From Fig. 11a, it is clear that the evolving melt will experience progressive depletion in light REE, Th, U, Nb and Ta, whereas large-ion lithophile elements (K, Rb, Sr, Ba and Pb) and mantle-compatible lithophile elements (Sc, V and, to some extent, heavy REE) will remain unaffected by the fractionation. The most dramatic changes will occur in the ratios of incompatible elements that are neither fractionated during low-degree melting in the mantle nor affected by fractionation of ferromagnesian phases, but have different compatibility with respect to perovskite (e.g., Nb vs. Ta or Th, or Th vs. U). Fig. 11b–d further illustrate the outcome of perovskite fractionation for the HFSE and REE budget of kimberlites and katungites. Even if we assume that the starting melt composition departed from that of the average kimberlite and katungite (i.e. the calculated evolutionary paths would start elsewhere on these diagrams), the observed variation in key element ratios for the entire dataset, or any of its parts, cannot be feasibly explained by perovskite fractionation. Even very small levels of F_{Prv} (on the order of 0.5 wt.%) should produce a distinct trend toward higher Nb/Ta and Nb/Th values, but very low La/Yb and Th/U values, at essentially constant Zr/Hf and Y/Ho ratios. No such trend is observed.

Table 5
Perovskite-groundmass partitioning data for kimberlites calculated by modeling perovskite zoning.

	Chicken Park	Iron Mountain	Udach. East 128 m	Udach. East 420 m
Ca site:				
Na[a]	1.5(4)	13(1)	2.6(5)	0.7(2)
K	0.0085(8)	0.012(2)	0.005(1)	0.0088(5)
Rb	0.0005(1)	0.0005(4)	0.0007(2)	0.0005(4)
Ca[a]	4.5(1)	5.00(6)	3.2(1)	4.0(2)
Mn	0.168(4)	0.12(1)	0.0600(1)	0.055(1)
Zn	0.021(3)	0.02(2)	0.0124(4)	0.012(7)
Sr	1.287(5)	2.65(8)	0.54(3)	0.57(2)
Ba	0.007(1)	0.017(3)	0.0021(2)	0.0025(2)
Pb	5(1)	14(3)	3(2)	6(2)
Y	12.93(8)	7.1(5)	7.4(3)	7.5(2)
La	43(1)	26.0(9)	28.6(9)	31.0(8)
Ce	52(2)	33(1)	36(1)	42(2)
Pr	63(2)	41(2)	45.7(8)	52(4)
Nd	66(2)	45(2)	48.1(6)	58(6)
Sm	58(2)	37(2)	41.7(8)	45(3)
Eu	49.7(8)	27(1)	29(1)	32.4(7)
Gd	40.4(7)	23(1)	27(2)	27.1(2)
Tb	28.4(9)	16(1)	18(1)	18.8(5)
Dy	28.0(6)	14(1)	16(1)	15.8(2)
Ho	21.0(3)	12.5(7)	12(1)	13.2(1)
Er	15.3(3)	8.2(9)	8(1)	8.3(2)
Tm	10.6(2)	5.0(8)	5.6(3)	4.9(3)
Yb	6.6(1)	3.3(5)	3.2(3)	2.9(2)
Lu	4.5(1)	2.9(8)	2.3(2)	2.1(2)
Th	101(29)	148(43)	153(39)	254(83)
U	14.3(8)	14(2)	21.2(8)	22(4)
Ti site:				
Al	0.087(3)	0.067(3)	0.034(5)	0.024(5)
Sc[b]	0.337(2)	0.19(4)	0.18(2)	0.14(3)
V	0.49(6)	0.89(4)	0.308(5)	0.28(4)
Fe	0.107(2)	0.13(1)	0.16(2)	0.143(6)
Ga	0.1292)	0.16(4)	0.07(2)	0.081(3)
Ti[a]	16.2(3)	15.6(3)	14.0(9)	15.5(9)
Zr	1.26(2)	1.1(2)	1.3(3)	1.5(3)
Hf	2.45(8)	2.0(3)	2.7(9)	3.2(6)
Nb	15.6(4)	14(2)	15(1)	18.0(2)
Ta	54(2)	63(9)	121(16)	113(21)

[a] The partition coefficients for Na, Ca and Ti values were calculated from WDS data and for the rest of the elements, from LA-ICP-MS data.

[b] The assignment of Sc to the Ti site is tentative; synthetic perovskites with Sc in both cation sites (e.g., $LaScO_3$ and $ScAlO_3$) are known.

The dependence of element partitioning on the redox conditions during crystallization is poorly understood for most minerals, including perovskite. In several recent studies, the Fe content of perovskite is used to estimate $f(O_2)$ values and relate these data to the evolution of kimberlitic magma and diamond preservation (e.g., Ogilvie-Harris et al., 2009; Sarkar et al., 2011). Although an increase in $f(O_2)$ will undoubtedly result in the increased availability of Fe^{3+} and, intuitively, higher Fe contents in perovskite (Chakhmouradian and Mitchell, 2001; Bellis and Canil, 2007), the approach taken in the aforementioned studies is too simplistic to be of much practical value. First of all, it does not take into account alternative mechanisms of Fe incorporation in perovskite (e.g., $Ca^{2+} + Ti^{4+} \Leftrightarrow REE^{3+} + Fe^{3+}$), which may contribute a significant proportion of the total Fe content in this mineral

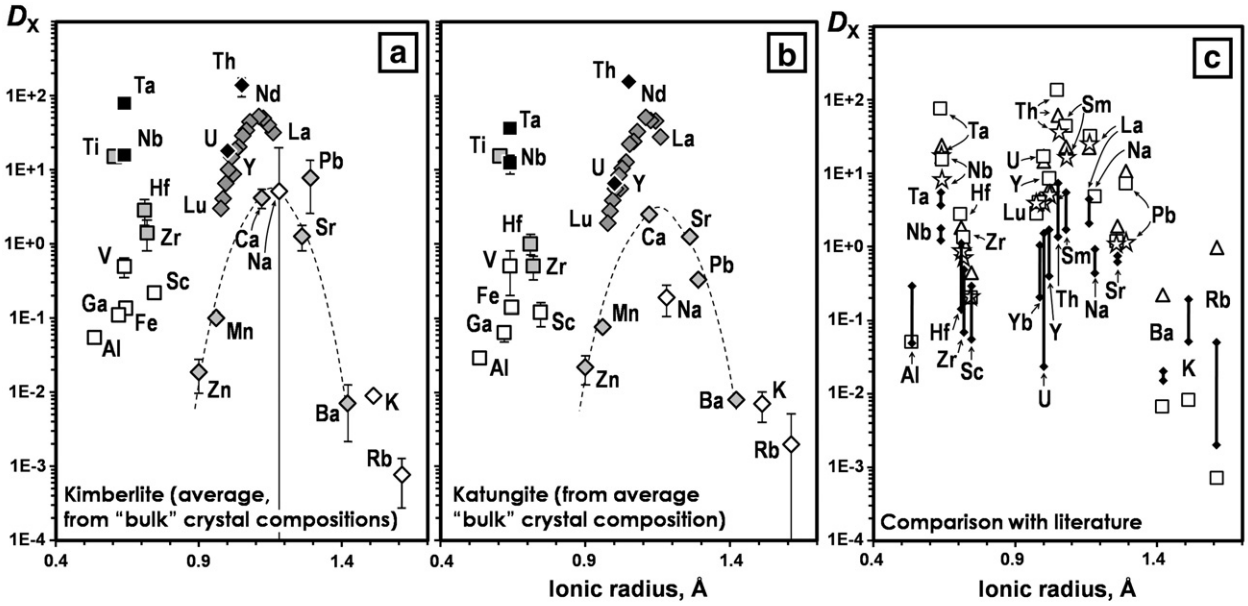

Fig. 10. Relations between the ionic radii of different elements in the Ca and Ti sites (diamonds and squares, respectively) and their perovskite-groundmass partition coefficients D_X (Table 4) in kimberlites (a) and katungite (b). Error bars are not shown where smaller than the size of the symbol. Note higher-than-expected partition coefficients for Na and Pb in kimberlitic perovskite. In (c), partition coefficients for selected elements from the present work (kimberlites only, squares) are compared with the data of Corgne and Wood (2005, vertical bars), Melluso et al. (2008, triangles) and Beyer et al. (2013–this volume).

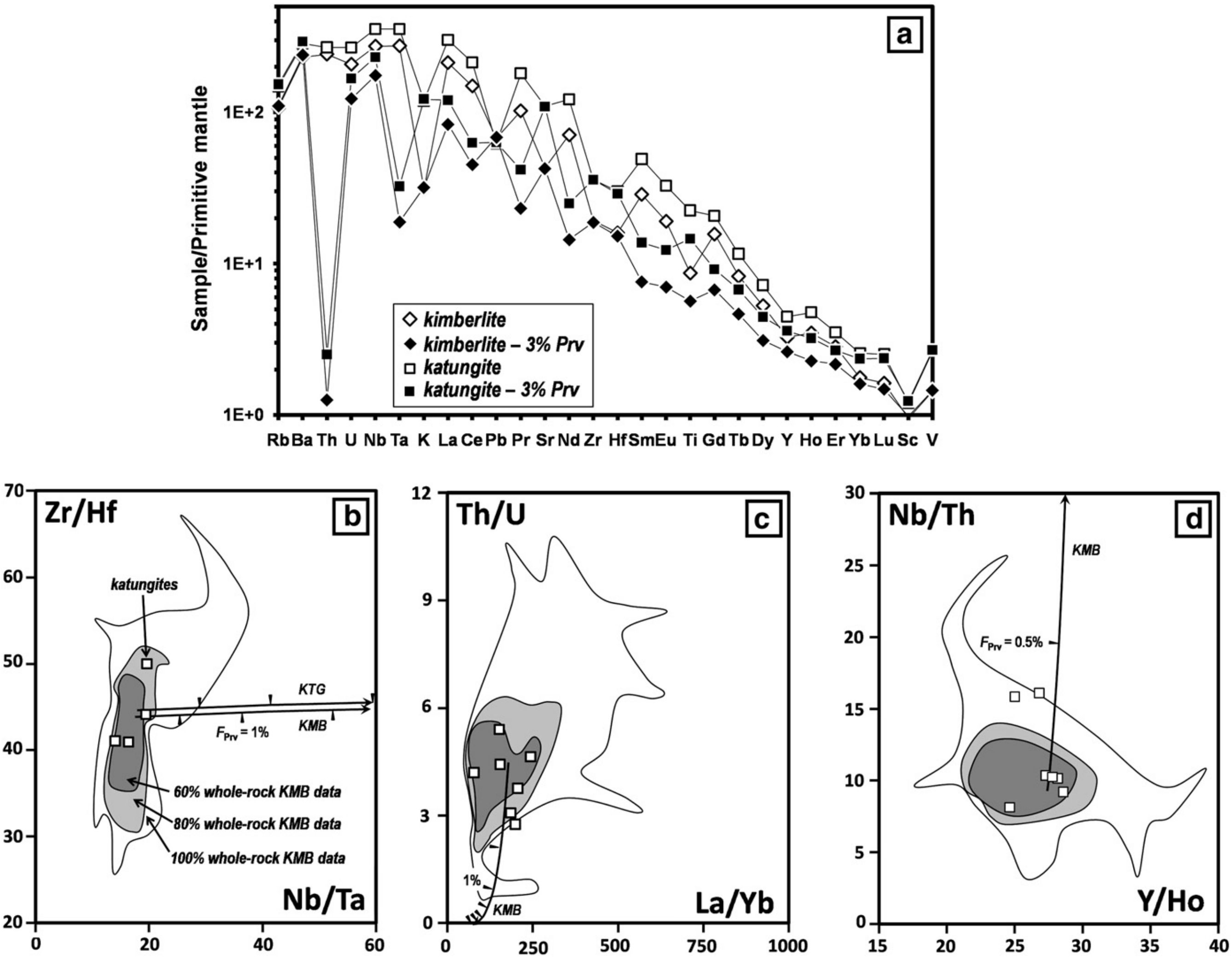

($>$10 mol%: Chakhmouradian and Mitchell, 2001). Secondly, it neglects the crystal-chemical controls over Fe partitioning. Note that Fe is a readily available element in most magmas, whereas Nb, Ta and REE are trace elements that, unlike Fe, are strongly compatible in perovskite. If Na or other elements capable of coupling with Nb, Ta and REE to maintain the balance of charge (e.g., $Ca^{2+}+Ti^{4+} \Leftrightarrow Na^{+}+HFSE^{5+}$, $2Ca^{2+} \Leftrightarrow REE^{3+}+Na^{+}$) are unavailable, the incorporation of Fe in perovskite will be controlled, to a large extent, by its Nb, Ta and REE contents, i.e. by redox-independent parameters (see Section 3.3). Note, in that context, that Na is moderately incompatible in perovskite, but its concentration decreases concomitantly with the REE, Th and Ta contents (e.g., Figs. 3a and 5a). It seems obvious that the Na enrichment in the core of zoned perovskite crystals is driven not by the high compatibility of this element, but by charge constraints, i.e. the need for coupled substitutions allowing highly charged *and highly compatible* cations to substitute for Ca and Ti (e.g., $3Ca^{2+} \Leftrightarrow Th^{4+}+2Na^{+}$; $Ca^{2+}+Ti^{4+} \Leftrightarrow Na^{+}+Ta^{5+}$).

In addition to enrichment in Fe, an increase in $f(O_2)$ should lead to a decrease in U and V levels owing to lower compatibility of small U^{6+} and V^{4+} in the Ca and Ti sites, respectively. These changes should also be accompanied by an increase in Mn content owing to substitution of Mn^{3+} and Mn^{4+} in the Ti site (e.g., Kulkarni et al., 2008; Pike and Slater, 2012). However, the trace-element data discussed in Sections 3.2 and 3.3 reveal no obvious correlation among these redox-sensitive elements (Figs. 3e and f), further attesting to the complexity of Fe-incorporation mechanisms in natural perovskite. In contrast to the findings of Ogilvie-Harris et al., 2009, our published (Chakhmouradian and Mitchell, 2001; this work) and unpublished data indicate no clear correlation between the Fe content in perovskite and the diamond content of its host kimberlite. In fact, the Lac de Gras kimberlites, well known for their overall high diamond potential, contain perovskite with some of the highest Fe levels ever reported (e.g., Table 1). The diversity of atomic substitutions in perovskite and the complexity of structural and paragenetic controls over Fe partitioning (see above) make any experimental attempt to constrain the intensive parameters of Fe incorporation susceptible to uncertainty.

Supplementary data to this article can be found online at http://dx.doi.org/10.1016/j.chemgeo.2013.01.007.

Acknowledgments

This work was supported by the Natural Sciences and Engineering Research Council of Canada (ARC, EPR), Canada Foundation for Innovation (ARC), and Australian Research Council (Professorial Fellowship and Discovery Grant to VSK). Numerous discussions of kimberlite petrology with Roger H. Mitchell (Lakehead University) helped us precipitate some of the ideas presented here; Roger is also thanked for his field guidance at Chicken Park and Iron Mountain, and his detailed comments on the previous version of this manuscript. It further benefitted from constructive reviews by Stephan Klemme, Ilya Veksler and Guest Editor Sebastian Tappe. We are also grateful to Leonid Danyushevsky (University of Tasmania) and Ravinder Sidhu (University of Manitoba) for their expert help with the data acquisition. Andrey Gurenko (Centre de Recherches Pétrographiques et Géochimiques, Nancy) is cordially thanked for sharing his unpublished whole-rock data on the Bunyaruguru katungite. BHP Billiton is acknowledged for providing the Grizzly kimberlite sample used in the present work.

References

Adam, J., Green, T., 2006. Trace element partitioning between mica- and amphibole-bearing garnet lherzolite and hydrous basanitic melt: 1. Experimental results and the investigation of controls on partitioning behavior. Contributions to Mineralogy and Petrology 152, 1–17.

Adam, J., Green, T., Sie, S.H., Ryan, C.G., 1997. Trace element partitioning between aqueous fluids, silicate melts and minerals. European Journal of Mineralogy 9, 569–584.

Armstrong, J.P., Wilson, M., Barnett, R.L., Nowicki, T., Kjarsgaard, B.A., 2004. Mineralogy of primary carbonate-bearing hypabyssal kimberlite, Lac de Gras, Slave Province, Northwest Territories, Canada. Lithos 76, 415–433.

Arndt, N.T., Guitreau, M., Boullier, A.-M., le Roex, A., Tommasi, A., Cordier, P., Sobolev, A., 2010. Olivine, and the origin of kimberlite. Journal of Petrology 51, 573–602.

Arzamastsev, A.A., Bea, F., Glaznev, V.N., Arzamastseva, L.V., Montero, P., 2001. Kola alkaline province in the Paleozoic: evaluation of primary mantle magma composition and magma generation conditions. Russian Journal of Earth Sciences 3, 1–35.

Batumike, J.M., Griffin, W.L., Belousova, E.A., Pearson, N.J., O'Reilly, S.Y., Shee, S.R., 2008. LAM-ICPMS U – Pb dating of kimberlitic perovskite: Eocene–Oligocene kimberlites from the Kundelungu Plateau, D.R. Congo. Earth and Planetary Science Letters 267, 609–619.

Bau, M., 1996. Controls on the fractionation of isovalent trace elements in magmatic and aqueous systems: evidence from Y/Ho, Zr/Hf, and lanthanide tetrad effect. Contributions to Mineralogy and Petrology 123, 323–333.

Bellis, A.J., Canil, D., 2007. Ferric iron in $CaTiO_3$ perovskite as an oxygen barometer for kimberlitic magmas I: experimental calibration. Journal of Petrology 48, 219–230.

Beyer, C., Berndt, J., Tappe, S., Klemme, S., 2013. Trace element partitioning between perovskite and kimberlite to carbonatite melt: New experimental constraints. Chemical Geology 353, 132–139 (this volume).

Blundy, J.D., Wood, B.J., 1994. Prediction of crystal-melt partition coefficients from elastic moduli. Nature 372, 452–454.

Boven, A., Pasteels, P., Punzalan, L.E., Yambaz, T.K., Musisi, J.H., 1998. Quaternary perpotassic magmatism in Uganda (Tore-Ankole Volcanic Province): age assessment and significance for magmatic evolution along the East African Rift. Journal of African Earth Sciences 26, 463–476.

Brey, G.P., Bulatov, V.K., Girnis, A.V., 2008. Geobarometry for peridotites: experiments in simple and natural systems from 6 to 10 GPa. Journal of Petrology 49, 3–24.

Brod, J.A., Barbosa, E.S.R., Junqueira-Brod, T.C., Gaspar, J.C., Diniz-Pinto, H.S., Sgarbi, P.B.A., Petrinovic, I.A., 2005. The Late-Cretaceous Goiás alkaline Province (GAP), Central Brazil. In: Comin-Chiaramonti, P., Gomes, C.B. (Eds.), Mesozoic to Cenozoic alkaline magmatism in the Brazilian Platform. Edusp/Fapesp, São Paulo, pp. 261–316.

Brooker, R.A., Sparks, R.S.J., Kavanagh, J.L., Field, M., 2011. The volatile content of hypabyssal kimberlite magmas: some constraints from experiments on natural rock compositions. Bulletin of Volcanology 73, 959–981.

Brown, I.D., Altermatt, D., 1985. Bond-valence parameters obtained from a systematic analysis of the inorganic crystal structure database. Acta Crystallographica B41, 244–247.

Chakhmouradian, A.R., Mitchell, R.H., 1999. Niobian ilmenite, hydroxylapatite and sulfatian monazite: alternative hosts for incompatible elements in calcite kimberlite at Internatsional'naya, Yakutia. The Canadian Mineralogist 37, 1177–1189.

Chakhmouradian, A.R., Mitchell, R.H., 2000. Occurrence, compositional variation and alteration of perovskite in kimberlites. The Canadian Mineralogist 38, 975–994.

Chakhmouradian, A.R., Mitchell, R.H., 2001. Three compositional varieties of perovskite from kimberlites of the Lac de Gras field (Northwest Territories, Canada). Mineralogical Magazine 65, 133–148.

Chakhmouradian, A.R., Mitchell, R.H., Pankov, A.V., Chukanov, N.V., 1999. Loparite and 'metaloparite' from the Burpala alkaline complex, Baikal Alkaline Province (Russia). Mineralogical Magazine 63, 519–534.

Chakhmouradian, A.R., Reguir, E.P., Mitchell, R.H., 2002. Strontium–apatite: new occurrences, and the extent of Sr-for-Ca substitution in apatite-group minerals. The Canadian Mineralogist 40, 121–136.

Choppin, G.R., 2002. Covalency in f-element bonds. Journal of Alloys and Compounds 344, 55–59.

Corgne, A., Wood, B.J., 2005. Trace element partitioning and substitution mechanisms in calcium perovskites. Contributions to Mineralogy and Petrology 149, 85–97.

Corgne, A., Liebske, C., Wood, B.J., Rubie, D.C., Frost, D.J., 2005. Silicate perovskite-melt partitioning of trace elements and geochemical signature of a deep perovskitic reservoir. Geochimica et Cosmochimica Acta 69, 485–496.

Dale, I.M., Henderson, P., 1972. The partition of transition elements in phenocryst-bearing basalts and the implications about melt structure. 24th Int. Geol. Congress, Section 10, pp. 105–111.

Donatti-Filho, J.P., Tappe, S., Oliveira, E.P., Heaman, L.M., 2013. Age and origin of the Neoproterozoic Brauna kimberlites: Melt generation within the metasomatized base of the São Francisco craton, Brazil. Chemical Geology 353, 19–35 (this volume).

Fig. 11. Compositional effects of perovskite partitioning on magma composition. (a) Changes in the concentration of selected trace elements (normalized to the primitive mantle of McDonough and Sun, 1995) in kimberlitic and katungitic magma affected by fractionation of 3 wt.% of perovskite; (b–d) changes in selected trace-element ratios expressed as fractionation trends, with tick marks spaced 0.5 wt.% of fractionating perovskite apart. As shown in (b), fractionation trends for kimberlites (KMB) and katungites (KTG) are essentially identical due to their geochemical similarity; the KTG trend is omitted from (c) and (d). To avoid clutter, the whole-rock data distribution for kimberlites is shown as contoured fields. The number of points in the 60% contour differs slightly in each diagram (100–105) owing to limited availability of data for some of the elements.

Eby, G.N., Lloyd, F.E., Woolley, A.R., Stoppa, F., Weaver, S.D., 2003. Geochemistry and mantle source(s) for carbonatitic and potassic lavas, Western Branch of the East-African Rift System, SW Uganda. Geolines 15, 23–27.

Eccles, D.R., Heaman, L.M., Luth, R.W., Creaser, R.A., 2004. Petrogenesis of the Late Cretaceous northern Alberta kimberlite province. Lithos 76, 435–459.

Edgar, A.D., Charbonneau, H.E., 1993. Melting experiments on a SiO2-poor aphanitic kimberlite from 5–10 GPa and their bearing on source of kimberlite magmas. American Mineralogist 78, 132–142.

Fedortchouk, Y., Zhang, Z., 2011. Diamond resorption: link to metasomatic events in the mantle or record of magmatic fluid in kimberlitic magma? The Canadian Mineralogist 49, 707–719.

Foley, S.F., Venturelli, G., Green, D.H., Toscani, L., 1987. The ultrapotassic rocks: characteristics, classification, and constraints for petrogenetic models. Earth-Science Reviews 24, 81–134.

Gaetani, G.A., Kent, A.J.R., Grove, T.L., Hutcheon, I.D., Stolper, E.M., 2003. Mineral/melt partitioning of trace elements during hydrous peridotite partial melting. Contributions to Mineralogy and Petrology 145, 391–405.

Gopalakrishnan, J., Uma, S., Bhat, V., 1993. Synthesis of layered perovskite oxides, $ACa_{2-x}La_xNb_{3-x}Ti_xO_{10}$ (A = K, Rb, Cs), and characterization of new solid acids, $HCa_{2-x}La_xNb_{3-x}Ti_xO_{10}$ ($0<x\le 2$), exhibiting variable Bronsted acidity. Chemistry of Materials 5, 132–136.

Hartman, P., Perdok, W.G., 1955. On the relations between structure and morphology of crystals. I. Acta Crystallographica 8, 49–52.

Heaman, L.M., Kjarsgaard, B.A., 2000. Timing of eastern North American kimberlite magmatism: continental extension of the Great Meteor hotspot track? Earth and Planetary Science Letters 178, 253–268.

Heaman, L.M., Kjarsgaard, B.A., Creaser, R.A., 2004. The temporal evolution of North American kimberlites. Lithos 76, 377–397.

Herd, C.D.K., Dwarzski, R.E., Shearer, C.K., 2009. The behavior of Co and Ni in olivine in planetary basalts: an experimental investigation. American Mineralogist 94, 244–255.

Hoernle, K., Schmincke, H.-U., 1993. The petrology of the tholeiites through melilitite nephelinites on Gran Canaria, Canary Islands: crystal fractionation, accumulation, and depths of melting. Journal of Petrology 34, 573–597.

Holmes, A., 1950. Petrogenesis of katungite and its associates. American Mineralogist 35, 772–792.

Horn, I., Foley, S.F., Jackson, S.E., Jenner, G.A., 1994. Experimentally determined partitioning of high field strength- and selected transition elements between spinel and basaltic melt. Chemical Geology 117, 193–218.

Janney, P.E., le Roex, A.P., Carlson, R.W., Viljoen, K.S., 2002. A chemical multi-isotope study of the Western Cape olivine melilitite province, South Africa: implications for the sources of kimberlites and the origin HIMU signature in Africa. Journal of Petrology 43, 2339–2370.

Kamenetsky, V.S., Maas, R., Kamenetsky, M.B., Paton, C., Phillips, D., Golovin, A.V., Gornova, M.A., 2004. Chlorine from the mantle: Magmatic halides in the Udachnaya-East kimberlite, Siberia. Earth and Planetary Science Letters 285, 96–104.

Kamenetsky, V.S., Kamenetsky, M.B., Sobolev, A.V., Golovin, A.V., Demouchy, S., Faure, K., Sharygin, V.V., Kuzmin, D.V., 2008. Olivine in the Udachnaya-East kimberlite (Yakutia, Russia): types, compositions and origins. Journal of Petrology 49, 823–839.

Keller, J., Zaitsev, A.N., Wiedenmann, D., 2006. Primary magmas at Oldoinyo Lengai: the role of olivine melilitites. Lithos 91, 150–172.

Keshav, S., Corgne, A., Gudfinnsson, G.H., Bizimis, M., McDonough, W.F., Fei, Y., 2005. Kimberlite petrogenesis: insights from clinopyroxene-melt partitioning experiments at 6 GPa in the CaO – MgO – Al2O3 – SiO2 – CO2 system. Geochimica et Cosmochimica Acta 69, 2829–2845.

Kinny, P.D., Griffin, W.L., Heaman, L.M., Brakhfogel, F.F., Spetsius, Z.V., 1997. SHRIMP U – Pb ages of perovskite from Yakutian kimberlites. Russian Geology and Geophysics 38, 97–105.

Kjarsgaard, B.A., Person, D.G., Tappe, S., Nowell, G.M., Dowall, D.P., 2009. Geochemistry of hypabyssal kimberlites from Lac de Gras, Canada: comparisons to a global database and applications to the parent magma problem. Lithos 112S, 236–248.

Klauer, S., Wöhlecke, M., 1994. Incorporation of hydrogen in cubic and uniaxial oxidic crystals deduced from polarized Raman scattering. Physical Review B 49, 158–181.

Kulkarni, V., Priolkar, K.R., Sarode, P.R., Rawat, R., Banerjee, A., Emura, S., 2008. Effect of Ti^{4+} substitution on structural, transport and magnetic properties of $La_{0.67}Sr_{0.33}Mn_{1-x}Ti_xO_3$. Journal of Physics: Condensed Matter 20, 1–12.

Le Roex, A.P., Bell, D.R., Davis, P., 2003. Petrogenesis of Group I Kimberlites from Kimberley, South Africa: evidence from bulk-rock Geochemistry. Journal of Petrology 44, 2261–2286.

Leeman, W.P., Scheidegger, K.F., 1977. Olivine/liquid distribution coefficients and a test for crystal–liquid equilibrium. Earth and Planetary Science Letters 35, 247–257.

Li, Q.-L., Li, X.-H., Liu, Y., Wu, F.-Y., Yang, J.-H., Mitchell, R.H., 2010. Precise U – Pb and Th – Pb age determination of kimberlitic perovskites by secondary ion mass spectrometry. Chemical Geology 269, 396–405.

McDonough, W.F., Sun, S.-s, 1995. The composition of the Earth. Chemical Geology 120, 223–253.

Melluso, L., Lustrino, M., Ruberti, E., Brotzu, P., De Barros Gomes, C., Morbidelli, L., Morra, V., Svisero, D.P., D'Amelio, F., 2008. Major- and trace-element composition of olivine, perovskite, clinopyroxene, Cr – Fe – Ti oxides, phlogopite and host kamafugites and kimberlites, Alto Paranaíba, Brazil. Can. Min. 46, 19–40.

Mitchell, R.H., 2004. Experimental studies at 5–12 GPa of the Ondermatjie hypabyssal kimberlite. Lithos 76, 551–564.

Mitchell, R.H., Bell, K., 1976. Rare earth element geochemistry of Potassie lavas from the Birunga and Toro-Ankole Regions of Uganda, Africa. Contributions to Mineralogy and Petrology 58, 293–303.

Mizuno, M., 1979. Phase diagrams of the systems $Al_2O_3-Ho_2O_3$ and $Al_2O_3-Er_2O_3$ at high temperatures. Yogyo Kyokaishi 87, 405–412.

Moreira, M.L., Paris, E.C., do Nascimento, G.S., Longo, V.M., Sambrano, J.R., Mastelaro, V.R., Bernardi, M.I.B., Andrés, J., Varela, J.A., Longo, E., 2009. Structural and optical properties of CaTiO3 perovskite-based materials obtained by microwave-assisted hydrothermal synthesis: an experimental and theoretical insight. Acta Materialia 57, 5174–5185.

Nagasawa, H., Schreiber, H.D., Blanchard, D.P., 1976. Partition coefficients of REE and Sc in perovskite, melilite, and spinel and their implications for Allende inclusions. Abstr. Lunar Planet. Sci. Conf., 7, pp. 588–590.

Nielsen, R.L., Gallahan, W.E., Newberger, F., 1992. Experimentally determined mineral-melt partition coefficients for Sc, Y and REE for olivine, orthopyroxene, pigeonite, magnetite and ilmenite. Contributions to Mineralogy and Petrology 110, 488–499.

Ogilvie-Harris, R.C., Field, M., Sparks, R.S.J., Walter, M.J., 2009. Perovskite from the Dutoitspan kimberlite, Kimberley, South Africa: implications for magmatic processes. Mining Magazine 73, 915–928.

Onuma, N., Ninomiya, S., Nagasawa, H., 1981. Mineral/groundmass partition coefficients for nepheline, melilite, clinopyroxene and perovskite in melilitenepheline basalt, Nyiragongo, Zaire. Geochemical Journal 15, 221–228.

Pasteris, J.D., 1980. The significance of groundmass ilmenite and megacryst ilmenite in kimberlites. Contributions to Mineralogy and Petrology 75, 315–325.

Pasteris, J.D., 1983. Kimberlites: A look into the Earth's mantle. American Scientist 71, 282–288.

Paton, C., Hergt, J.M., Phillips, D., Woodhead, J.D., Shee, S.R., 2007. New insights into the genesis of Indian kimberlites from the Dharwar Craton via *in situ* S isotope analysis of groundmass perovskite. Geol. 35, 1011–1014.

Paton, C., Hergt, J.M., Woodhead, J.D., Phillips, D., Shee, S., 2009. Identifying the asthenospheric component of kimberlite magmas from the Dharwar Craton, India. Lithos 112S, 296–310.

Patterson, M., Francis, D., McCandless, T., 2009. Kimberlites: Magmas or mixtures? Lithos 112S, 191–200.

Pearce, S.F., Russel, J.K., Kopylova, M.G., 1997. Primitive magma from the Jericho pipe, N.W.T., Canada: Constraints on primary kimberlite melt chemistry. Journal of Petrology 41, 789–808.

Peterson, T.D., 1989. Peralakline nephelinites. I. Comparative petrology of Shombole and Oldoinyo L'engai, East Africa. Contributions to Mineralogy and Petrology 101, 458–478.

Pike, T.W., Slater, P.R., 2012. Synthesis of new Mn/Ti containing perovskites and examination of their potential use as solid oxide fuel cell electrodes. Internationa Journal of Low-Carbon Technologies 7, 60–62.

Pontes, D.S.L., Longo, E., Pontes, E.M., Galhiane, M.S., Santos, L.S., Pereira-da-Silva, M.A., da Silva, J.H.D., Chiquito, A.J., Pizani, P.S., 2009. Effects of strontium and calcium simultaneous substitution on electrical and structural properties of $Pb_{1\text{-}x\text{-}y}Ca_xSr_yTiO_3$ thin films. Applied Physics A 96, 731–740.

Price, S.E., Russell, J.K., Kopylova, M.G., 2000. Primitive Magma From the Jericho Pipe, N.W.T., Canada: Constraints on Primary Kimberlite Melt Chemistry. Journal of Petrology 41, 789–808.

Reguir, E.P., Chakhmouradian, A.R., Halden, N.M., Yang, P., Zaitsev, A.N., 2008. Early magmatic and reaction-induced trends in magnetite from the carbonatites of Kerimasi, Tanzania. The Canadian Mineralogist 46, 879–900.

Robles-Cruz, S.E., Watangua, M., Isidoro, L., Melgarejo, J.C., Galí, S., Olimpio, A., 2009. Contrasting compositions and textures of ilmenite in the Catoca kimberlite, Angola, and implications in exploration for diamond. Lithos 112S, 966–975.

Rosenthal, A., Foley, S.F., Pearson, D.G., Nowell, G.M., Tappe, S., 2009. Petrogenesis of strongly alkaline primitive volcanic rocks at the propagating tip of the western branch of the East African Rift. Earth and Planetary Science Letters 284, 236–248.

Sarkar, C., Storey, C.D., Hawkesworth, C.J., Sparks, R.S.J., 2011. Degassing in kimberlite: Oxygen isotope ratios in perovskites from explosive and hypabyssal kimberlites. Earth and Planetary Science Letters 312, 291–299.

Shannon, R.D., 1976. Revised effective ionic radii and systematic studies of interatomic distances in halides and chalcogenides. Acta Crystallographica A32, 751–767.

Simon, S.B., Kuehner, S.M., Davis, A.M., Grossman, L., Johnson, M.L., Burnett, D.S., 1994. Experimental studies of trace element partitioning in ca, Al-rich compositions: Anorthite and perovskite. Geochimica et Cosmochimica Acta 58, 1507–1523.

Skinner, E.M.W., Marsh, J.S., 2004. Distinct kimberlite pipe classes with constraining eruption processes. Lithos 76, 183–200.

Smith, C.B., Sims, K., Chimuka, L., Duffin, A., Beard, A.D., Townend, R., 2004. Kimberlite metasomatism at Murowa and Sese pipes, Zimbabwe. Lithos 76, 219–232.

Sobolev, A.V., Sobolev, S.V., Kuzmin, D.V., Malitch, K.N., Petrunin, A.G., 2009. Siberian meimechites: origin and relation to flood basalts and kimberlites. Russian Geology and Geophysics 50, 999–1033.

Sparks, R.S.J., Brooker, R.A., Field, M., Kavanagh, J., Schumacher, J.C., Walter, M.J., White, J., 2009. The nature of erupting kimberlite melts. Lithos 112S, 429–438.

Tanaka, K., Takahashi, Y., Shimizu, H., 2008. Local structure of Y and Ho in calcite and its relevance to Y fractionation from Ho in partitioning between calcite and aqueous solution. Chemical Geology 248, 104–113.

Tappe, S., Foley, S.F., Pearson, D.G., 2003. The kamafugites of Uganda: a mineralogical and geochemical comparison with their Italian and Brazilian analogues. Periodico di Mineralogia 52, 51–77.

Tappe, S., Steenfelt, A., Nielsen, T., 2012. Asthenospheric source of Neoproterozoic and Mesozoic kimberlites from the North Atlantic craton, West Greenland: new high-precision U – Pb and Sr – Nd isotope data on perovskite. Chemical Geology 320–321, 113–127.

Ulrych, J., Lloyd, F.E., Balogh, K., 2003. Age relations and geochemical constraints of Cenozoic alkaline volcanic rock series in W Bohemia: a review. GeoLines 15, 168–180.

Upton, B.G.J., Mitchell, R.H., Logs, A., Aspen, P., 1992. Primitive olivine melanephelinite dykes from the Orkney Islands, Scotland. Geological Magazine 129, 319–324.

Weber, M.J., Bass, M., Andringa, K., Monchamp, R.R., Comperchio, E., 1969. Czochralski growth and properties of $YAlO_3$ laser crystals. Applied Physics Letters 15, 342–345.

Wilson, S.A., 1997. The collection, preparation, and testing of USGS reference material BCR-2, Columbia River Basalt. USGS Open-File Report.

Wilson, M., Rosenbaum, J.M., Dunworth, E.A., 1995. Melilitites: artial melts of the thermal boundary layer? Contributions to Mineralogy and Petrology 119, 181–196.

Wood, B.J., Blundy, J.D., 2002. The effect of H2O on crystal-melt partitioning of trace elements. Geochimica et Cosmochimica Acta 66, 3647–3656.

Woodhead, J., Hergt, J., Phillips, D., Paton, C., 2009. African kimberlites revisited: in situ Sr-isotope analysis of groundmass perovskite. Lithos 112, 311–317.

Wu, F.Y., Yang, Y.H., Mitchell, R.H., Li, Q.L., Yang, J.H., Zhang, Y.B., 2010. In situ U – Pb age determination and Nd isotopic analysis of perovskites from kimberlites in southern Africa and Somerset Island, Canada. Lithos 115, 205–222.

Wu, F.Y., Mitchell, R.H., Li, Q.L., Sun, J., Liu, C.Z., Yang, Y.H., 2013. In situ U–Pb age determination and Sr-Nd isotopic analysis of perovskite from the Premier (Cullinan) kimberlite, South Africa. Chemical Geology 353, 83–95 (this issue).

Wyatt, B.A., Baumgartner, M., Anckar, E., Grutter, H., 2004. Compositional classification of “kimberlitic” and “non-kimberlitic” ilmenite. Lithos 77, 819–840.

Yang, Y.-H., Wu, F.-Y., Wilde, S.A., Liu, X.-M., Zhang, Y.-B., Xie, L.-W., Yang, J.-H., 2009. In situ perovskite Sr – Nd isotopic constraints on the petrogenesis of the Ordovician Mengyin kimberlites in the North China Craton. Chemical Geology 264, 24–42.